I. GEBAUER

M.S.

2005

This is to certify that the
thesis entitled

A MONTE CARLO STUDY OF DIFFERENT DETECTOR GEOMETRIES FOR HAWC

presented by

IRIS GEBAUER

has been accepted towards fulfillment
of the requirements for the

M.S. degree in Physics and Astronomy

James T. Linnemann
Major Professor's Signature

August 24, 2005
Date

A MONTE CARLO STUDY OF DIFFERENT DETECTOR GEOMETRIES FOR HAWC

By

Iris Gebauer

A THESIS

Submitted to
Michigan State University
in partial fulfillment of the requirements
for the degree of

MASTER OF SCIENCE

Department of Physics and Astronomy

2005

ABSTRACT

A MONTE CARLO STUDY OF DIFFERENT DETECTOR GEOMETRIES FOR HAWC

By

Iris Gebauer

Compared to other parts of astronomy the study of the universe at energies above 100GeV is a relatively new field. Pointed instruments presently achieve the highest sensitivities. They have detected gamma-rays from at least 10 sources, but they are only able to monitor a relatively small fraction of the sky. The detection of exciting phenomena such as Gamma-ray Bursts (GRBs) requires a highly sensitive detector capable of continuously monitoring the entire overhead sky. Such an instrument could make an unbiased study of the entire field of view. With sufficient sensitivity it could detect short transients ($\sim$ 15 minutes) and study the time structure of Active galactic nuclei (AGN) flares at energies unattainable to space-based instruments. This thesis describes the design and performance of the next generation water Cherenkov detector HAWC (High Altitude Water Cherenkov). Focussing on the performance in background-rejection and sensitivity to point sources, two possible detector geometries, different in the way the photomultipliers (PMTs) are separated from each other, are compared.

ACKNOWLEDGEMENTS

I would like to thank Brenda Dingus for mentoring and assisting me during my time in Los Alamos, as well as Gus Sinnis and Curtis Lansdell for their constant input and support. Aous Abdo deserves special thanks for keeping me warm in Lansing. I also would like to acknowledge a scholarship and further financial support of the German National Academic Foundation (Studienstiftung des deutschen Volkes).

TABLE OF CONTENTS

LIST OF TABLES

LIST OF FIGURES

Images in this thesis are presented in color.

1 Introduction

1.1 Motivation for γ-Ray Astronomy

Before experiments could detect gamma rays emitted by cosmic sources, it was known that the universe should be producing these photons. Work by Feenberg and Primakoff in 1948, Hayakawa and Hutchinson in 1952, and, especially, Morrison in 1958 had led to the belief that a number of different processes would result in gamma-ray emission. These processes included cosmic ray interactions with interstellar gas, supernova explosions, and interactions of energetic electrons with magnetic fields. Balloon-borne hard X-ray and gamma-ray imaging telescopes provided the first images of the sky in the energy range 20-1000 keV. They discovered black hole candidate sources in the galactic center region, first imaged the cobalt-decay gamma-rays from the supernova SN 1987A, and provided the first capability to localize high-energy sources for comparison with more detailed lower-energy X-ray observations.

Significant gamma-ray emission from our galaxy was first detected in 1967 by the gamma-ray detector aboard the OSO-3 satellite. It detected 621 events attributable to cosmic gamma-rays. The satellites SAS-2 (1972) and the COS-B (1975-1982) confirmed earlier findings of a galactic gamma-ray background, produced the first detailed map of the sky at gamma-ray wavelengths, and detected a number of point sources. However, the poor resolution of the instruments made it impossible to identify most of these point sources with known objects.

Perhaps the most spectacular discovery in gamma-ray astronomy came in the late 1960s and early 1970s from a constellation of defense satellites which were put into orbit for a completely different reason. Detectors on board the Vela satellite series, designed to detect flashes of gamma-rays from nuclear bomb blasts, began to record bursts of gamma-rays – not from the vicinity of the Earth, but from deep space.

Today, these gamma-ray bursts are seen to last for fractions of a second to minutes. Studied for over 25 years now with instruments on board a variety of satellites and space probes, and ground-based instruments, the sources of these high-energy flashes remain unknown. They appear to be of extragalactic origin, and currently the most likely theory seems to be that at least some of them come from so-called hypernova explosions - supernovas creating black holes rather than neutron stars. The Swift spacecraft was launched in November, 2004. It is designed to provide rapid location and follow-up for a large sample of gamma-ray bursts.

For the most energetic part of the gamma-ray spectrum, ground-based experiments are suitable. The Imaging Atmospheric Cherenkov Telescope technique currently achieves the highest sensitivity. The Crab Nebula, a steady source of TeV gamma-rays, was first detected in 1989 by the Whipple Observatory (Az, USA) and later confirmed by seven ground-based telescopes, including the water-cherenkov-detector Milagro. Modern Cherenkov telescope experiments like H.E.S.S., VERITAS, MAGIC, and CANGAROO III can detect the Crab Nebula in a few minutes. The most energetic photons (up to 16 TeV) observed from an extragalactic object originate from the blazar Markarian 501 (Mrk 501). These measurements were done by the High-Energy-Gamma-Ray Astronomy (HEGRA) air Cherenkov telescopes.

Gamma-ray astronomy is mostly dominated by the number of photons that can be detected. Larger area detectors and better background suppression are essential for progress in the field (see section 5).

The observation of the universe in gamma-rays opens a window to some of the most extreme environments which are invisible to ordinary telescopes. Some specific targets include: Gamma-ray Bursts, Black Holes and Neutron Stars, Supernovae, Pulsars, Diffuse Emission, Active Galaxies and Unidentified Sources.

1.2 Cosmic Rays

Figure 1 shows the cosmic ray energy spectrum. Below 10^{16}eV the spectrum can be fitted with a power law with spectral index -2.7, above this value the energy-dependence becomes $E^{-3.0}$. The turning-point, known as the knee, has a flux of about 1 particle per square meter and year. A second change in the gradient of the curve occurs at 10^{19} eV, known as the ankle, where the spectrum becomes less steep once again. Cosmic ray particles are most likely accelerated by diffusive shock acceleration in strong shock fronts of supernova remnants. The model first introduced by Fermi [16] ("2nd order Fermi-acceleration") has been extended and modified by many authors (see, e.g. [8], [9], [14], [15] and [10]). In these models particles are deflected by moving magnetized clouds. Particles cross the shock front several times and thereby gain energy up to the PeV region. Fermi acceleration at strong shocks leads to a power-law spectrum close to the observed one.

However, there must be a limiting energy that can be achieved in this process: when a particle's energy reaches the value at which its gyro-radius in the magnetic field is greater than the dimensions of the accelerating regions, it will inevitably escape. The presence of the knee in the spectrum could be caused by different effects.

First, it could indicate that that two distinct sources are responsible for the acceleration of particles below and above it. The lower energy part might be described by the supernova acceleration, the origin of the higher energetic part of the spectrum is unknown, although many theories exist. The most accepted of these is acceleration in active galactic nuclei (AGN).

Second, energy dependent losses occurring during the propagation through the interstellar medium could be responsible for the change of the spectral index. Processes like spallation, leakage from he galaxy, nuclear decay, ionization losses and, for low energies, solar modulation can modify the energy spectrum during the diffuse

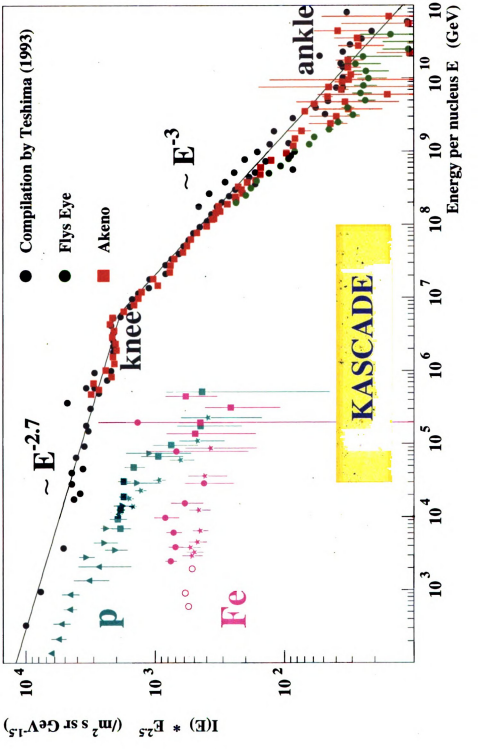

Figure 1: The spectrum of cosmic rays. Taken from [27].

propagation of the particles through the galaxy.

Third, a change in the elemental composition of the cosmic rays could cause the steepening [4].

Fourth, new interaction characteristics owing to new particle physics at energies $s^{1/2}$ above 1TeV $nucleon^{-1}$ [4].

And fifth, an observational bias related to the change in the experimental techniques from direct particle-by-particle balloon and spacecraft experiments below $\sim 10^{14}$ eV to indirect ground-based air shower measurements above 10^{15} eV [4].

Below 10^{19} eV it is not possible to trace particles back to their sources, even if the arrival direction on earth is known. The trajectories of these particles are completely scrambled by the galactic magnetic field, since, even at these energies, the gyro-radius in the galactic field is smaller than the size of the galaxy. Assuming a magnetic field of 1G and a galactic radius of 50.000Ly the gyro-radius of a proton becomes comparable to the radius of the Milky Way at energies above 10^{19}eV.

No phenomenon in the neighborhood of our galaxy can account for cosmic rays with energies up to 10^{19}, yet their sources may not lie much further away, because otherwise the Greisen-Zatsepin-Ku'zmin (GZK)-cutoff needs to be taken into account: Space is filled with the cosmic microwave background (CMB) radiation, a relic of the epoch of recombination when the first hydrogen-atoms formed. There are about 10^9 of these photons in a cubic meter of space, yet normally a cosmic ray particle will be oblivious to their presence. Things change however when a cosmic ray proton has so much energy that in its own reference frame the CMB photon's energy is sufficient to cause the Δ-excitation:

$$p + \gamma_{CMB} \longrightarrow \Delta^+ + X \longrightarrow \{ \begin{matrix} n + \pi^+ \\ p + \pi^0 \end{matrix} , for\ E_p - p \cdot cos\theta \geq \frac{m_p m_\pi}{q},$$

with E_p: energy of the proton in center-of-mass system, p: absolute value of the proton's momentum in center-of-mass system, θ: angle under which the proton hits the photon, , q: absolute value of the photon's momentum in center-of-mass system, m_p: proton-mass, m_π: pion-mass. The universe becomes opaque for cosmic-ray protons when this resonant reaction with comic microwave background radiation photons becomes energetically allowed. The excited state then decays by the two channels shown. Naturally the resulting particles will have to share the energy, thus none will have an energy as great as the original one. This is called the GZK cutoff. The reaction above is possible when the proton's energy is greater than $5 \cdot 10^{19}$ eV. Such a proton is expected to be reduced to an energy below the cutoff over a distance of 50 Mpc. Note that cosmic ray nuclei will be broken up by interactions with CMB at lower energies. Particles with energies above the cutoff have been detected none the less, despite the lack of known sources within range.

At low energies the cosmic ray spectrum mainly consists of protons and light elements. The fraction of heavier elements increases with increasing energy significantly. At around 100GeV protons make up about 56% of the cosmic rays, helium 24% and heavier elements 20%. At 1PeV the spectrum consists of about 15% protons, 33% helium and 52% heavier elements [26].

1.3 Hadronic and Electromagnetic Air Showers

When cosmic rays arrive at earth, they interact in the atmosphere, provided that the cosmic ray-particles are not deflected or captured by the Earth's magnetic field. The latter occurs if the energy of a charged particle exceeds $\sim$ 10 GeV. A cosmic ray particle will interact with a nucleus in the atmosphere (primarily oxygen and nitrogen). This is referred to as the primary interaction and typically occurs at an altitude of about 15-20km.

The primary interaction causes both the nucleus and the cosmic ray particle to fragment into a number of hadrons such as kaons, pions, neutrons and protons and light nuclei as well as a number of more exotic particles.

Due to the conservation of momentum these particles continue along the path of the original particle, with a small spread in the transverse direction. Some will fragment further and others will decay. Both charged pions and kaons decay into a muon and a neutrino, while neutral pions decay into a pair of photons. The photons can initiate electromagnetic cascades: they produce electron-positron pairs, which in turn can produce more photons through bremsstrahlung. The process continues as long as there is enough energy to create more particles. Figure 2 shows a simulation of a hadronic cascade.

Photon-initiated cascades, on the other hand, are completely electromagnetic, thus showing a significantly different appearance of the shower front at sea level. For a gamma ray of energy larger than 10 MeV the dominant interaction as it enters the atmosphere is pair production. On the average this will occur after it traverses one radiation length of atmosphere, i. e. at an altitude of 29km. The resulting electron positron pair will share the energy of the primary gamma ray and will be emitted in forward direction [17]. After another radiation length these secondary particles may also pair produce (see figure 3). On the average the number of particles doubles after each radiation length, leading to an average energy of $\frac{E}{2^N}$ per particle in the Nth generation, with E: the energy of the primary (0th generation).

The angle of emission in all these processes will be $\propto \frac{m_e c}{E}$ rad, where E is the energy of the electron and m_e is the rest mass of the electron [30]. Consequently the electromagnetic cascade will be strongly concentrated around the shower core. This process continues until the ionization energy losses and radiation energy losses are equal. At this point the cascade reaches the 'shower maximum'.

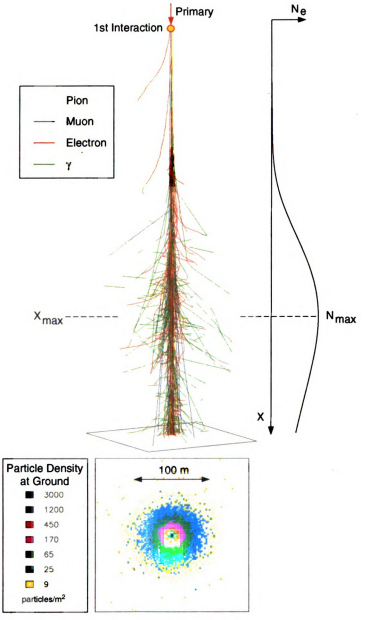

Figure 2: The simulated development of a 1 PeV air-shower. Only a small fraction of particles is shown. The right hand plot shows the evolution of the total particle number with depth. The lower figure shows the distribution of particles at ground level. Taken from [23].

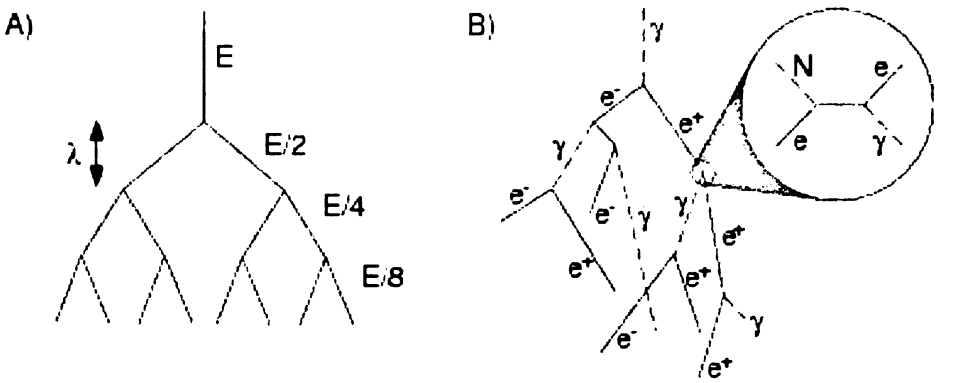

Figure 3: A) The 'toy model' picture of a cascade. B) A more realistic model of an electromagnetic cascade assuming $\lambda_{pair} \approx \frac{9}{7}\lambda_{brem.}$. Taken from [23].

From here on the number of particles gradually decreases and the cascade dies away. The altitude at which the shower maximum occurs depends on the energy of the primary particle. The observation altitude therefore changes the observed energy-range.

Energy E_γ	$X_{max}(g \cdot cm^{-2})$	$h_{max}(km)$	N_{max}	N_{sl}	N_{mt}
10 GeV	175	12.8	1.6×10^1	4×10^{-4}	2×10^{-2}
100 GeV	261	10.3	1.3×10^2	4×10^{-2}	1.4×10^0
1 TeV	346	8.4	1.1×10^3	3×10^0	6×10^1
10 TeV	431	6.8	1.0×10^4	1.3×10^2	1.7×10^3
100 TeV	517	5.5	9.3×10^4	4.5×10^3	3.6×10^4

Table 1: Gamma-ray shower parameters as a function of energy. The variables are explained in the text. Values taken from [30].

Table 1 shows the values N_{max}=maximum number of electrons, X_{max}=shower thickness traversed in $g \cdot cm^{-2}$, h_{max}=elevation of shower maximum, N_{sl}=number of surviving particles at sea level and N_{mt}= number of surviving particles at mountain

altitude (2300m) for typical gamma-ray primaries. The development of an electromagnetic cascade in comparison with a hadronic cascade is shown in figure 4. The particles in an air shower travel through the atmosphere at a velocity close to the speed of light. At a given moment or altitude the shower front can be visualized as a segment of a sphere (a disk with curvature), while the density of the particles in the center of the disk (shower core) is far greater than at large radii. As the shower propagates through the atmosphere the shower front expands. At ground level an electromagnetic shower is composed primarily of electrons, positrons and photons. The total number of particles in a gamma-ray-induced shower is approximately equal to the the energy of the primary one, expressed in GeV [30]. A 10^{19} eV shower involves on the order of 10 billion particles. These particles will be spread over an area that for the largest extensive air showers is tens of square-kilometers. Over the energy range of interest the charged cosmic radiation is $10^3 - 10^4$ times as numerous as the diffuse gamma-ray background. This means that, in the field of view of a simple telescope whose solid angle is optimized for gamma ray detection, the background of cosmic ray events is 10^3 times as numerous as the strongest steady gamma-ray source thus far detected. The arrival directions of the charged cosmic rays are isotropic, because of interstellar magnetic fields, therefore a discrete gamma-ray-source can only be detected as an anisotropy in an otherwise isotropic distribution of air showers. In order to detect a gamma-ray source in this way, it would have to be very strong (a few percent of the cosmic radiation). Fortunately there are a number of factors concerning the properties of hadronic showers and purely electromagnetic cascades that enable us to differentiate between hadronic and electromagnetic cascades and make the ground based study of cosmic sources of VHE gamma rays with air- and water-Cherenkov telescopes possible. The electromagnetic cascade consists almost entirely of electrons, positrons and photons. The hadronic cascade is initiated by a charged ion and the core of the cascade consists of the products of hadronic interactions. These feed lesser

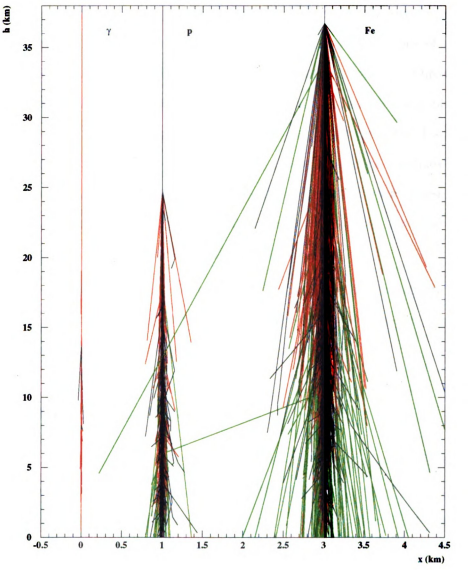

Figure 4: Development of the cascades of three different primaries through the atmosphere:green: muons, red: leptons, black: hadrons.Taken from [27].

electromagnetic cascades whose products are largely responsible for the emission of cherenkov light. Because a greater proportion of the energy in an electromagnetic cascade goes into particles that emit Cherenkov light, the typical Cherenkov light yield is two to three times that of a primary cosmic ray of the same energy. The hadron interactions in the core emit their secondary products at wider angles of emission than their electromagnetic counterparts, so that the hadronic cascade is broader and more scattered. The resulting Cherenkov light distribution in the focal plane of a detector is broader than for a gamma ray initiated air-shower and provides a simple method differentiating between the two. Some of the secondary particles emitted from the core are penetrating particles which can reach ground level. These, as well as the larger fluctuations in the development of the hadron shower, have the effect of increasing the fluctuations in the Cherenkov shower image.

Cosmic electrons also produce electromagnetic cascades. They constitute a small, but virtually irreducible, background. The background due to cosmic electrons is 100-1000 times smaller than the background due to protons.

1.4 Detection Technique

The Milagro observatory was the first water Cherenkov detector used for the detection of extensive air showers. In addition to the atmosphere the water acts as a large calorimeter which, because of its higher refractive index compared to air, lowers the threshold energy and raises the photon yield and the Cherenkov angle significantly. At ground level the diffraction index in air is $n = 1.00029$ and θ_{max} is 1.3^0. The threshold energy for electrons is 21MeV and the light yield in the visible range is about 30 photons m^{-1}. In water, where $n = 1.33$, θ_{max} is about 41^0 and the threshold energy for electrons is lowered to 260 keV, the Cherenkov photon yield is about 2500 photons m^{-1}, an increase by a factor of more than 80 compared to air [30]. Unlike

pointed instruments, an extensive air shower array (EAS) can monitor nearly the complete overhead sky continuously. Since it detects particles that penetrate to the ground level from each direction in the overhead sky it has a field of view that nearly covers the entire overhead sky. The observation of the Crab nebula and the active galaxies Mrk 421 and Mrk 501 by the first-generation-experiment Milagro proved, that the technique is sufficient to detect sources [6] and the influence and importance of high altitude has been demonstrated by the Tibet group [3].

A natural next step is the combination of both these properties: the all-sky and high-duty factor capabilities of Milagro, a lower energy threshold (due to high altitude) and an increased sensitivity (due to large area). As formulated in [29] reasonable design goals for such an experiment are:

-Ability to detect gamma-ray bursts to a red-shift of 1.0
-Ability to detect AGN to a red-shift beyond 0.3
-Ability to resolve AGN flare at the intensities and durations observed by the current generation of ACTs
-Ability to detect the Crab nebula in a single transit

This thesis describes two slightly different designs for a next generation all-sky VHE gamma-ray telescope, the HAWC (High Altitude Water Cherenkov) array, that satisfies the above requirements. The required sensitivity demands a large area detector ($\sim 10^5\ m^2$). Because of the desired low energy threshold the detector needs to be placed at extreme altitude (above 4500m). At present two different sites for the HAWC-detector are discussed: A site at 4572 m in Yanbajing,Tibet and a site at 5200m in the Atacama desert in Chile. In this thesis only the Chile-altitude is discussed. For the simulations Milagro's latitude of about $35^o\ 5'$ north is used in order to enable comparison (see e.g section 7.1).

2 Air Shower Simulations

The analysis presented in this thesis is entirely based on Monte-Carlo (MC)-simulations. Two different programs are used: The program CORSIKA for the propagation of the cascade through the atmosphere and the program Geant for the propagation of the shower particles through the detector.

2.1 The Propagation of Air Showers through the Atmosphere with CORSIKA

CORSIKA (COsmic Ray SImulations for KAskade) is a program for simulation of extensive air showers initiated by high energy cosmic ray particles [21]. Possible primaries are protons, light nuclei up to iron, photons and other particles. For this analysis only photons and protons are considered as primaries. Since protons make up a large fraction of the cosmic rays this is a reasonable estimate of the cosmic ray background. Starting with the first interaction the particles are tracked through the atmosphere until they undergo reactions with the air nuclei or decay. The hadronic interactions at high energies can be described by five different interaction models. For this Monte Carlo simulation the VENUS option has been used, which is based on the Gribov-Regge-theory. In order to obtain enough statistics for a reasonable analysis millions of air showers have been thrown with the following parameters for proton and gamma primaries:

Energy-spectrum:

Energy-Range: 10GeV to 100TeV

Spectral index: -2.7 for protons and -2.4 for photons

Geometry of thrown range:

Thrown azimuth-angle-range: $0^o - 360^o$

Thrown zenith-angle-range: $0^o - 45^o$

Observation-level: 5200m

2.2 The Detector Simulation with Geant

The program Geant [18] is used in order to simulate the penetration of the shower particles through pond-cover and water. Input for Geant are the CORSIKA showers. The core positions are distributed randomly over a circle with radius 1km centered on the pond. The output of Geant includes, for each PMT that was hit by at least one photon, the number of photoelectrons (PEs) and their arrival times, it is therefore very similar to the calibrated data format of Milagro.

2.2.1 The HAWC-detector

The HAWC-detector consists of 11250 photomultiplier tubes (PMTs) arranged in a grid of 75x75 PMTs in a top- and 75x75 PMTs in a bottom-layer. With a horizontal PMT-spacing of 4m, a height of 1.5m of the bottom-layer above the ground, a distance of 4m between top- and bottom-layer and 2m of covering water above the top-layer the pond has a volume of 675,000 m^3, with a length and width of 300m and a depth of 7.5 m. As in the Milagro detector, tubes are planned to be aligned at sand filled PVC-tubes giving each tube only a small variation in height and horizontal direction. In order to prevent scattering of Cherenkov light by particles in the water, the water in the pond needs to be constantly cleaned by filters. The concrete on the ground and side-walls of the pond is modelled as a metal with 5% reflectivity, the pond cover

is also assumed to have 5% reflectivity.

2.2.2 The curtained geometry: Geom04

In this geometry half-height curtains, consisting of a material with 5% reflectivity, surrounding each PMT are added to the detector design. The curtains go from shortly above the top layer to the center of the pond. The aim is to prevent photons emitted from one particle from reaching two different PMTs thus causing a "shifted" image of the particle. In addition photons can be reflected from the PMT-case or the glass surface, the concrete floor and walls or the cover. Compared to baffles (see section 2.2.3) curtains are expected to lower the number of triggered events.

The PMTs are modelled by a volume with a diameter of 20.32cm and a height of 35cm. The glass is assumed to be 0.2cm thick with a diameter of 16.76cm.

The performance of curtained PMTs will be tested at the Milagro detector probably in fall 2005.

2.2.3 The baffled geometry: Geom05

In this detector setup cone-shaped baffles of 16.54cm height and a radius of 26.67cm at the top and 8.38cm at the bottom are added to each PMT. The material of the baffles is assumed to have an absorbtion probability of 95% on the outside and 2% on the inside. Similarly to the curtains, the main purpose of this adjustment is the prevention of multiple PMT hits and the detection of photons that have been reflected at other PMTs or concrete and cover. Baffles similar to the ones described above are currently in use in the Milagro-detector.

2.2.4 Data sample

With a trigger-condition of at least 55 PMTs hit in HAWC's top layer and at least 20 PMTs participating in the fit, the 4,294,285 thrown gamma-ray initiated showers led to 9300 triggered events and the 13,118,625 thrown proton-initiated showers led to 3,667 triggered events for geom04. For geom05 2,387,719 gamma-ray initiated showers where thrown, leading to 12,933 triggered events and 4,331,657 proton-initiated showers where thrown, leading to 4,277 triggered events.

3 Binning Analysis

Due to the high number of cosmic ray events, the analysis for HAWC consists of looking for an excess of gamma-ray events above the hadronic background. For a point source the presence of the large background and the finite angular resolution of the HAWC detector (0.28^o for geom04 and 0.35^o for geom05, see section 4.1) makes it necessary to subdivide the data into bins. An infinitely large bin would on the one hand include the excess from other possible point sources as well and on the other hand the signal would disappear in the large background. Without any background an infinitely large bin would keep all the signal events. An optimal bin size that, when centered directly on a point source, keeps as little background events and as much signal events from the source as possible, needs to be determined. The angular resolution of HAWC is a function of the number of tubes participating in the fit, N_{fit}. A higher N_{fit}-cut would throw away more poorly reconstructed events and therefore improve the angular resolution. Since most of the poorly reconstructed events would not have fallen into the signal bin an N_{fit}-cut leads to an increase in sensitivity as an N_{fit}-cut reduces the number of background events. The angular resolution in Milagro is usually quantified by two parameters out of which one can be considered as a theoretical" parameter which only applies to MC-data. This parameter, Δ_{angle}, is the space angle difference between the true direction of the shower front and the fitted direction of the shower front:

$$\Delta_{angle} = \Omega_{true} - \Omega_{fit}. \tag{1}$$

The second parameter, Δ_{EO}, does not depend on the true direction of the shower front. This parameter compares the the fitted directions of the shower front that are provided by two different parts of the detector: the detector is subdivided into a set of squares (each square centered around a PMT like the white and black squares of a

chessboard), of which the white fraction is used for one fit and the black fraction is used for another fit. Δ_{EO} is now the difference between the fit directions from from the two subset-fits. Since systematic errors are expected to affect both fits in the same way the difference between the two fits, Δ_{EO}, should be widely independent of the systematics. In the absence of systematic errors Δ_{EO} is expected to be about twice the angular resolution of the detector [2].

Because the angular resolution depends on the number of tubes participating in the fit, the optimal bins size and N_{fit} cannot be determined independently. The background spectrum can be assumed to be isotropic, so that the effect of a change in bin size is purely geometric: $\frac{p_1}{p_2} = \frac{r_1^2}{r_2^2}$, for a circular bin, where p_i is the number of protons in a bin of size r_i. For this analysis only circular bins are used. Square bins are easier to implement and only slightly inferior [2]. A decrease in bin size leads to a gain in sensitivity, since more background events are excluded until a point is reached where too many signal events are thrown out. The improvement in sensitivity is given by the relative Q-factor, defined as:

$$Q = \frac{\epsilon_{signal}}{\sqrt{\epsilon_{background}}}, \tag{2}$$

with ϵ_i is the fraction of events of type i kept after a certain cut (or set of cuts). This definition leads to

$$Q = \frac{n_{signal}(cuts)}{\sqrt{n_{bg}(cuts)}} \cdot \frac{\sqrt{n_{bg}(ref)}}{n_{signal}(ref)}, \tag{3}$$

where $n_i(cuts)$ is the number of events of type i kept after a certain set of cuts and $n_i(ref)$ is the number of events of type i kept after a set of reference cuts. In the case of γ/proton-separation (see section 5) this is the total number of triggered events that pass an N_{fit} cut.

In this case, where cuts in N_{fit} and r are applied the Q-factor can be written as

$$Q = \frac{n_{signal}(N_{fit}, r)}{\sqrt{n_{bg}(N_{fit}, r)}} \cdot \frac{\sqrt{n_{bg}(ref)}}{n_{signal}(ref)} = \frac{n_{signal}(N_{fit}, r)}{\sqrt{n_{bg}(N_{fit}, r)}} \cdot c, \tag{4}$$

where c is a constant factor that only depends on the reference point. The number $n_i(N_{fit}, r)$ is the number of events of type i which have at least N_{fit} tubes participating in the fit and $\Delta_{angle} \leq r$.

The assumption of a flat background immediately leads to

$$n_{bg} = n^o_{bg}(N_{fit}) \cdot \cdot r^2, \tag{5}$$

where $n^o_{bg}(N_{fit})$ is the number of background events in a bin with radius 1 for a given N_{fit} cut. Substituting eq. 5 into eq. 4 leads to:

$$Q = \frac{n_{signal}(N_{fit}, r)}{\sqrt{n_{bg}(N_{fit})} \cdot r} \cdot c. \tag{6}$$

The absolute value of Q is arbitrary, it depends on the set of reference cuts. In order to find the optimal bin size only the position of the maximum of the Q-factor distribution is of interest.

Figures 5 and 6 show the relative Q-factors versus bin radius for different N_{fit} cuts. The optimal bin sizes r=0.45 for geom04 and r=0.55 for geom05 and $N_{fit} = 20$ have been chosen as reference points. A higher N_{fit} cut leads to a smaller bin radius thus resulting in an improvement in angular resolution. In the range of $0 \leq N_{fit} \leq 50$, the variations of the relative Q-factor and of the fraction of photons kept are small, the value 20 was chosen for the analysis. This choice on the one hand eliminates the events with the poorest reconstruction, but on the other hand keeps a reasonable fraction of photons. Maximization of the Q-factor leads to an optimal bin size of

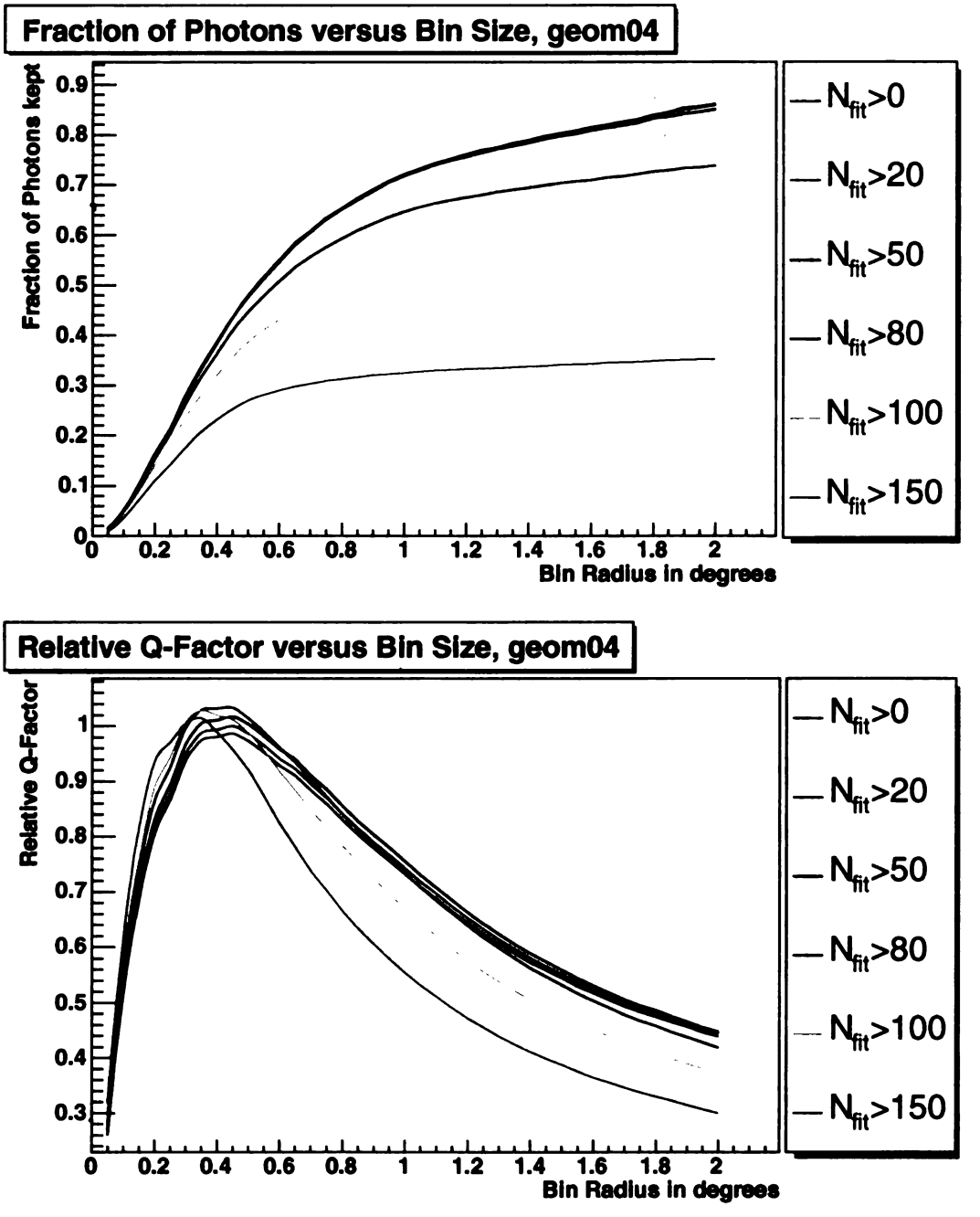

Figure 5: Top: The fraction of gammas kept after a cut in bin size for different cuts in N_{fit} for geom04. Bottom: The corresponding Q-factors.

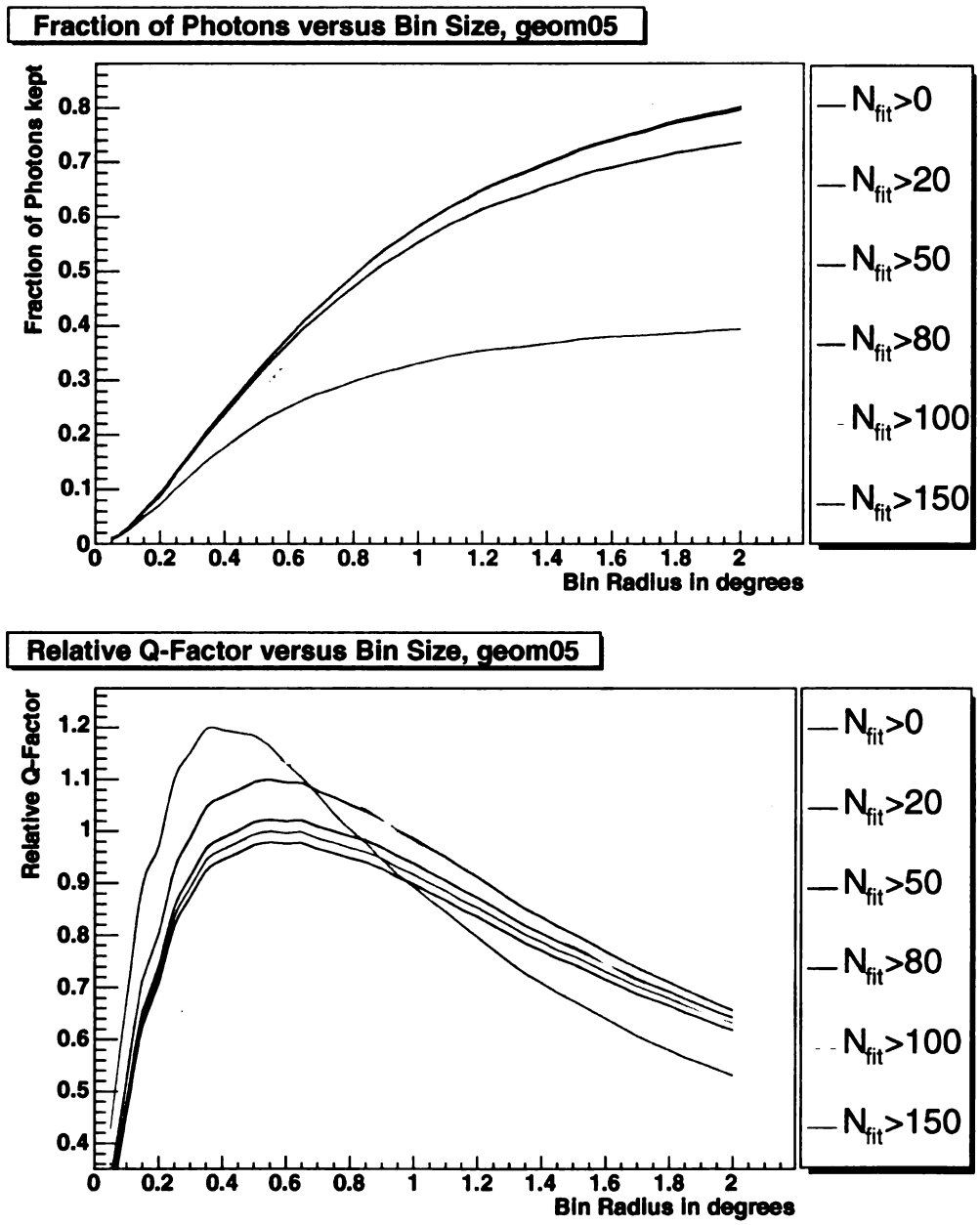

Figure 6: Top: The fraction of gammas kept after a cut in bin size for different cuts in N_{fit} for geom05. Bottom: The corresponding Q-factors.

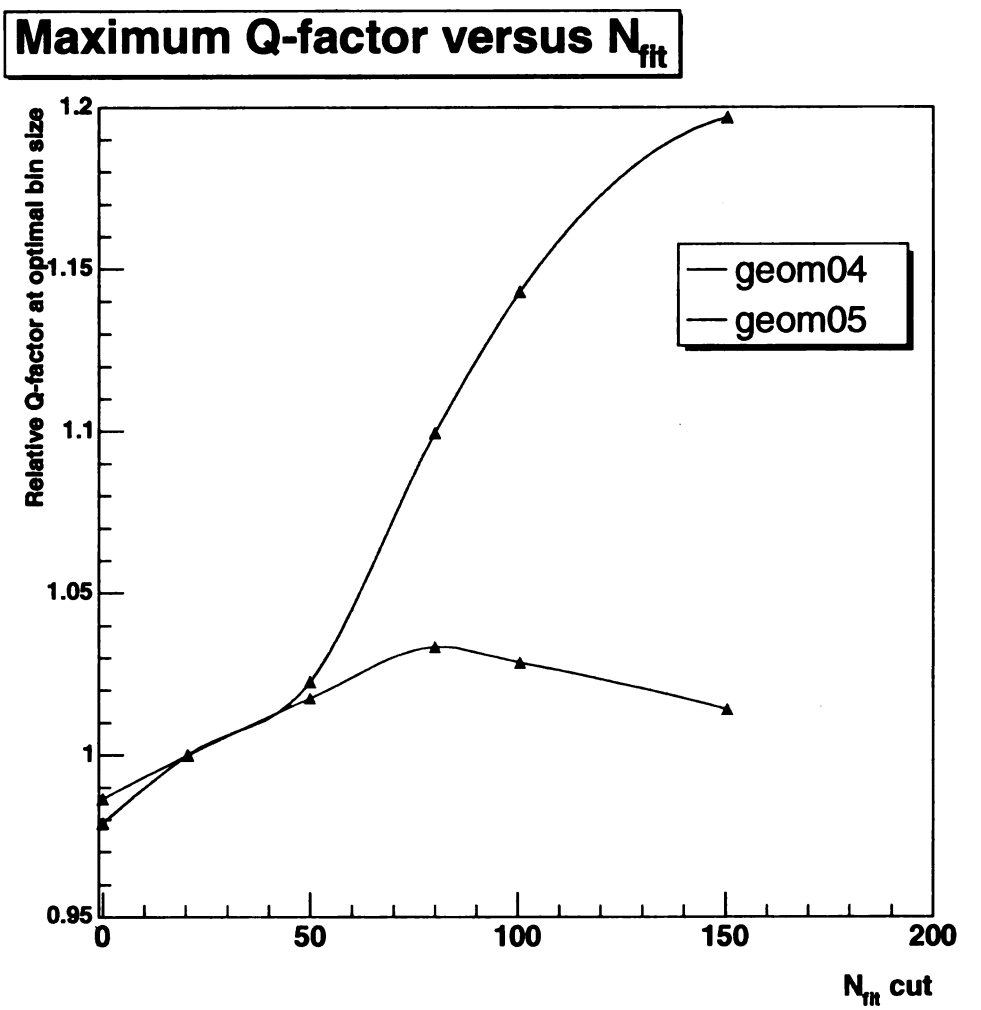

Figure 7: Maximum relative Q-factor (Q-factor corresponding to the optimal bin size) versus N_{fit}.

0.45 for geom04 and 0.55 for geom05. These values are expected to optimize the significance of a point source for the two geometries. As one can see from figure 5 and 6 these values keep about 44% of the signal events while throwing away about 18% of the background for geom04 and 35% of the signal events while throwing away about 19% of the background for geom05.

The difference in the detector geometries leads to a significantly different dependence of the maximum relative Q-factor on N_{fit} cuts. Figure 7 shows the maximum relative Q-factor versus N_{fit}. For geom04 the maximum relative Q-factor is maximal for an N_{fit} cut of 80. Higher and lower values of N_{fit} lead to lower Q-factors. For geom05 the maximum relative Q-factor rises with rising N_{fit} cut. Figure 7 suggests an N_{fit} cut of 80 for geom04 and 150 or higher for geom05. As discussed before such high N_{fit} cuts reduce the number of photons kept significantly.

4 Angular Reconstruction with HAWC

The relative arrival times at which the different PMTs in the detector are struck are used to reconstruct the direction of the incident shower. The fir includes a correction for curvature of the shower front and a so-called sampling-correction which takes into account that the shower front has a finite thickness the incident direction of the shower is determined by a weighted least squares fit.

It should be noted that the curvature corrections used in this analysis are the curvature corrections that have been optimized for the Milagro site, i.e. for Milagro's altitude and the size of the detector. Due to the higher altitude of the HAWC-detector and due to the larger area the detector covers, a different curvature of the shower front can be expected: Assuming the shower to cover a cone-shaped volume as it propagates through the atmosphere, the higher altitude and the larger detector cause HAWC to "see" a larger fraction of the shower in a different state of development, thus possibly leading to a different curvature.

4.1 Angular Resolution in HAWC

Under the assumption of a flat background spectrum the angular resolution can be estimated through

$$\frac{r}{1.58} = \sigma, \tag{7}$$

where r is the optimal bin size [2].Thus, the expected angular resolution for the two geometries is 0.28 degrees for geom04 and 0.35 degrees for geom05. Table 2 shows the optimal bin size and the resulting angular resolution for the two geometries.

Figure 8 shows the normalized Δ_{angle} distributions for both geometries. The full lines correspond to an N_{fit} cut of 20. For comparison the distributions for an N_{fit} cut of 100 are also shown (dotted lines). For both N_{fit} cuts the distribution for geom04

parameter:	geom04	geom05
optimal bin size r	0.45	0.55
angular resolution σ	0.28	0.35

Table 2: Angular resolution and optimal bin size of the two geometries

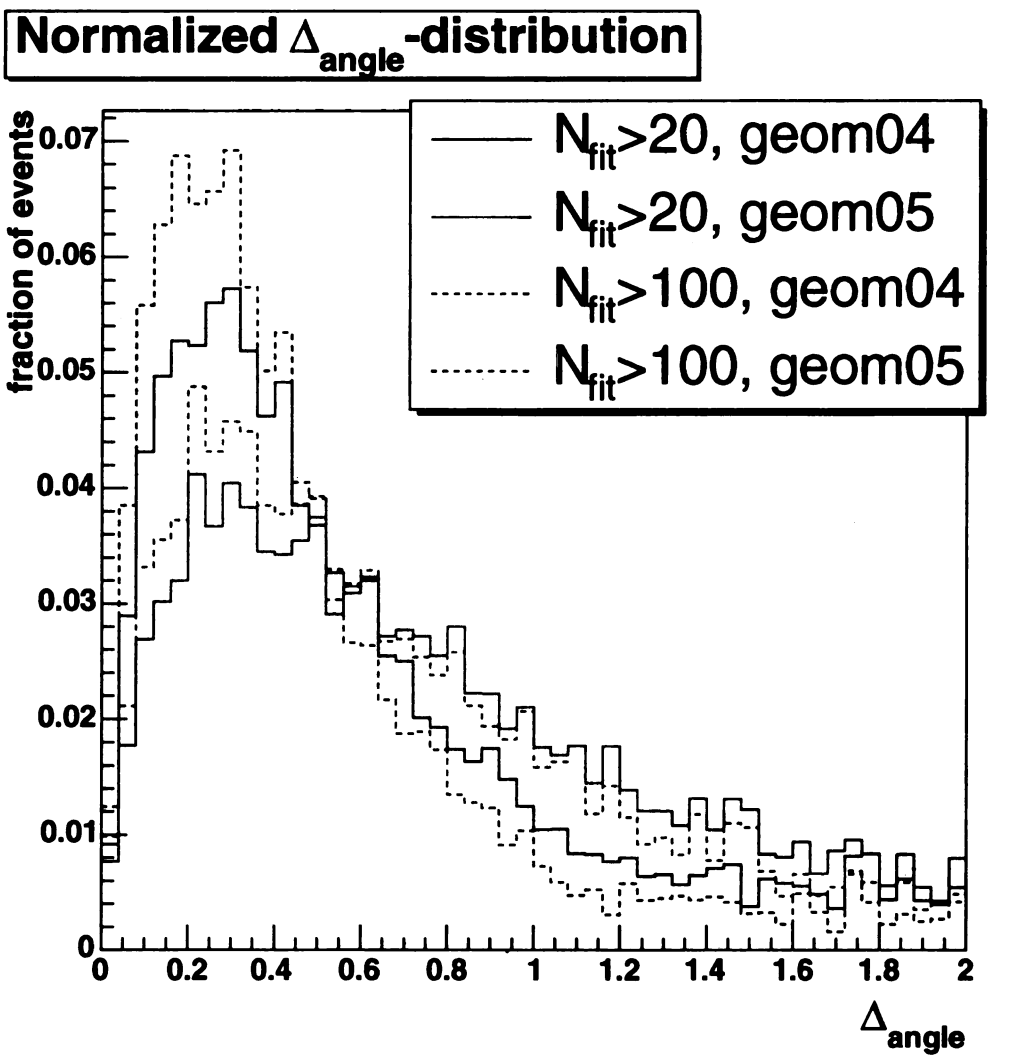

Figure 8: Normalized Δ_{angle} distribution for both geometries.

is shifted towards lower values in Δ_{angle} compared to geom05. The fraction of events at high values of Δ_{angle} is lower for geom04 than for geom05, thus leading to a better angular resolution for geom04. As discussed before (see section 3), a higher N_{fit} cut increases the angular resolution by reducing the number of poorly reconstructed events.

5 Gamma/hadron-Separation

5.1 Background Rejection in Milagro

Hadrons entering the atmosphere interact with nucleons in the air thus producing charged pions which then can decay into muons and neutrinos. Also high-energetic hadronic particles can reach ground-level. Gamma-rays in contrast interact with the nuclei in the air almost purely electromagnetic, leading to an air shower with mostly lower-energetic electrons, positrons and gamma rays. Because of their high mass compared to electrons, muons have great penetrating power, e.g. muons with energies above 1.2GeV (at observation level) reach the bottom layer of Milagro [6]. Muons that reach the bottom layer illuminate a small number of PMTs thus leading to a clustered image. Figure 9 shows six Monte-Carlo events imaged in the top- and bottom layer of HAWC.

During the 5 years of operation of the Milagro-Gamma-Ray-Observatory the Milagro-Collaboration has introduced several variables in order to differentiate between gamma and proton induced air showers. The additional water-calorimeter and the two separate layers of PMTs enable the detector to differentiate between the two possible shower types by looking at the number of muons in the shower. Additional information about the clumpiness and the physical size of the image has been implemented in different variables.

5.1.1 Compactness parameter

As described in the beginning of this section hadronic air showers lead to a number of hits in the bottom layer in a relatively confined region with a high number of photoelectrons in the PMTs. Electromagnetic cascades on the other hand lead to a more homogeneous distribution of hits with a lower number of PEs in the tubes. In

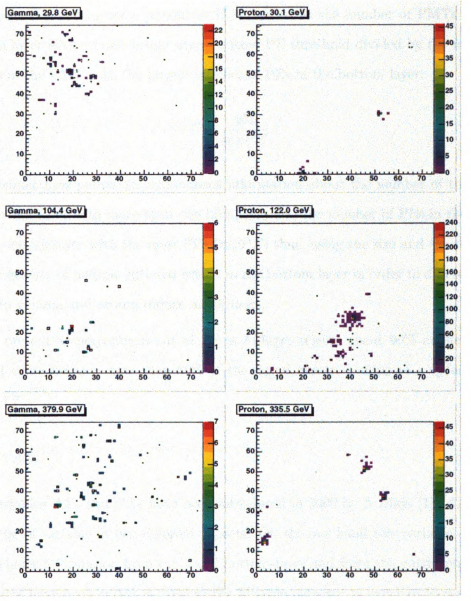

Figure 9: Three gamma-ray induced events (left) and proton induced events (right) as observed in geom04. The PMTs in top- and bottom-layer are superimposed: bottom-layer: color-scale, top-layer: black boxes. The size of the boxes and the color corresponds to the number of PEs in the PMT.

2003 the so called compactness parameter was introduced [6], a variable that combines these two properties in order to differentiate between hadronic and electromagnetic cascades. The compactness parameter C is defined as the number of PMTs in the bottom layer with a pulse height above a fixed PE threshold divided by the number of PEs in the PMT with the largest number of PEs in the bottom layer:

$$C = \frac{nb2}{mxPE}. \tag{8}$$

The compactness parameter summarizes information about the number of tubes in the bottom layer with more than two hits ($nb2$) and the number of PEs in the tube in the bottom layer with the most PEs ($mxPE$) thus, using the size and the relative inhomogeneity of hadron-initiated events in the bottom layer in order to differentiate between gamma and proton induce air showers.

At present a compactness cut of 2.5 in Milagro rejects about 90% of the background while keeping more than 50% of the signal events, leading to a Q-factor of about 1.7.

5.1.2 AX_4

The variables AX_4 and CX_2 have been introduced in 2005 by A.Abdo [1]. AX_4 is a new type of variable in two different aspects: On the one hand this variable -unlike C - includes information from top - and bottom-layer and from the outriggers. The outriggers have been added in 2003 to the Milagro detector in order to increase the angular resolution through a better core fit. On the other hand AX_4 is not a 'physical' variable in the sense that it has not been found by trying to implement the air showers properties in the variable. Instead a set of different variables was examined and their

performance in gamma/hadron separation compared. AX_4 is defined as:

$$AX_4 = \frac{N_{out} \cdot N_{fit} \cdot N_{top}}{cxPE}, \tag{9}$$

with

N_{out}: the number of outriggers hit,

N_{fit}: the number of PMTs entered in the fit,

N_{top}: the number of PMTs hit in the top layer and

$cxPE$: the number of PEs in the muon layer tube with the highest number of PEs where a region of 10m around the fitted shower core is excluded from consideration.

CX_2 is defined as

$$CX_2 = \frac{nb2}{cxPE}. \tag{10}$$

Two dimensional cuts in AX_4 and CX_2 have been applied, leading to Q-factors of 2.5 and more. The application of AX_4 and CX_2 to the Crab nebula increased the signal by a factor of 1.4 from 3.65σ (with a C-cut) to 5.05σ.

5.2 Background Rejection in HAWC

In the following I will compare the performance of the two parameters C and AX_4 in the two HAWC geometries. AX_4 has to be modified for the HAWC detector, because of the different detector geometry. The parameter C does not depend on the actual detector geometry, but in preliminary studies for different HAWC geometries a slight modification appeared to be more successful.

5.2.1 The new Compactness-parameter

The compactness-parameter for HAWC is defined as

$$C_H = \frac{N_{top}}{cxPE}, \tag{11}$$

with N_{top} as the number of struck PMTs in the top layer. Unlike C, this parameter now includes information from top and bottom layer.

Figure 10 shows the C_H-distribution for gamma and proton induced showers for the two geometries. For both geometries the proton events are mostly confined to a region $C_H < 10$, this region includes more than 90% of the events (see figure 11). The region including 90% of the gamma-events spreads out until $C_H \approx 25$. Figure 11 shows the fraction of Monte Carlo gamma primaries and Monte Carlo proton primaries with C_H-values larger than the x-axis-value. While the normalized gamma-distribution is very similar for both geometries, the proton-distribution spreads out further for geom05. Thus, for a C_H cut a better background rejection can be expected from geom04.

Figure 11 shows the fraction of Monte Carlo gamma primaries and Monte Carlo proton primaries with C_H-values larger than the x-axis-value.

Figure 12 shows the Q-factor as a function of C_H. For geom04 with a C_H-cut of 8, 65.5% of the signal events are kept while excluding 97.2% of the proton events, thus leading to a Q-factor of 3.344. For geom05 with an C_H-cut of 6.1, 79.0% of the signal events are kept while excluding 83.4% of the proton events, thus leading to a Q-factor of 1.94115.

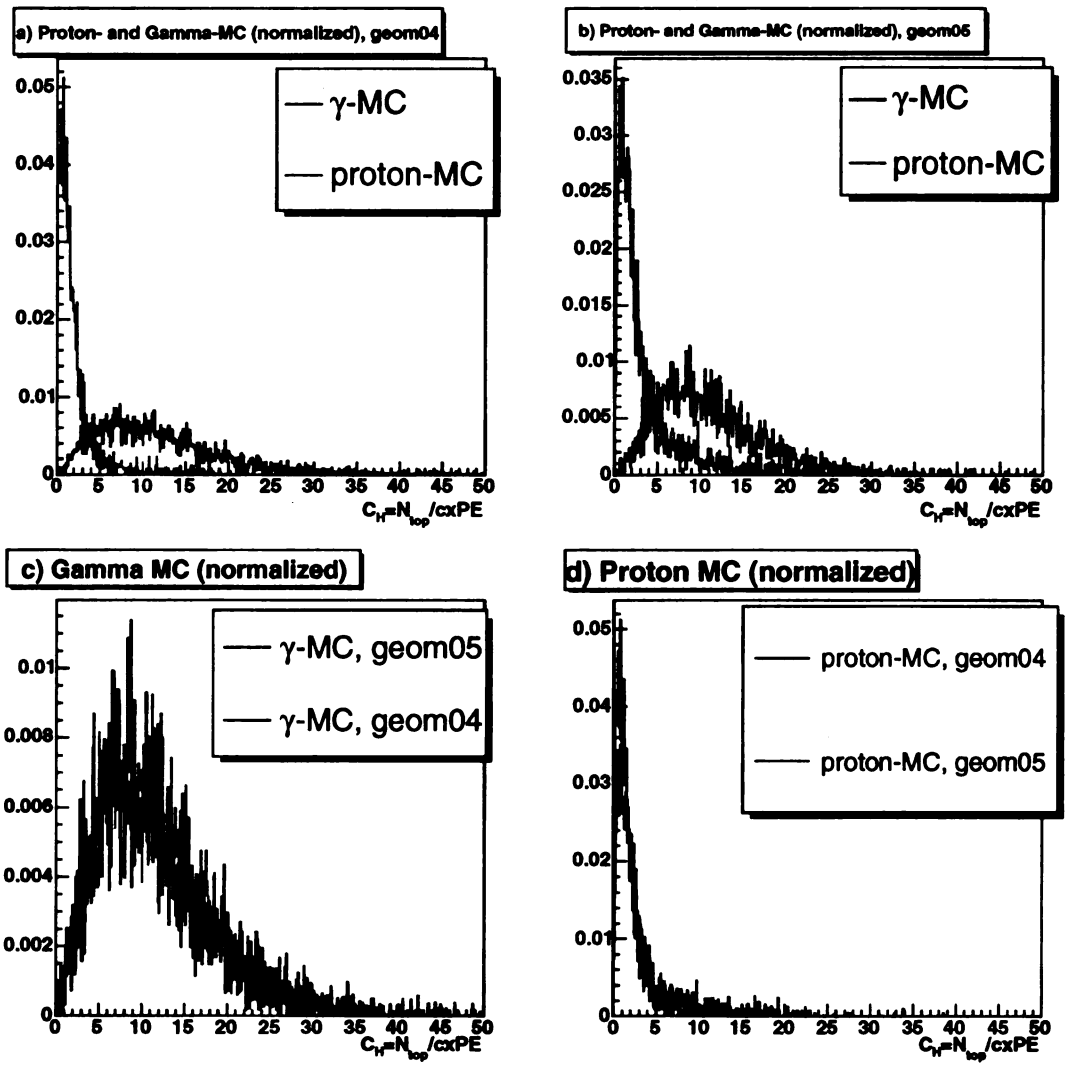

Figure 10: The normalized event distribution for both geometries in parameter space: a) for geom04 and both primaries, b) for geom05 and both primaries, c) for gamma-MC and both geometries, d) for proton-MC and both geometries.

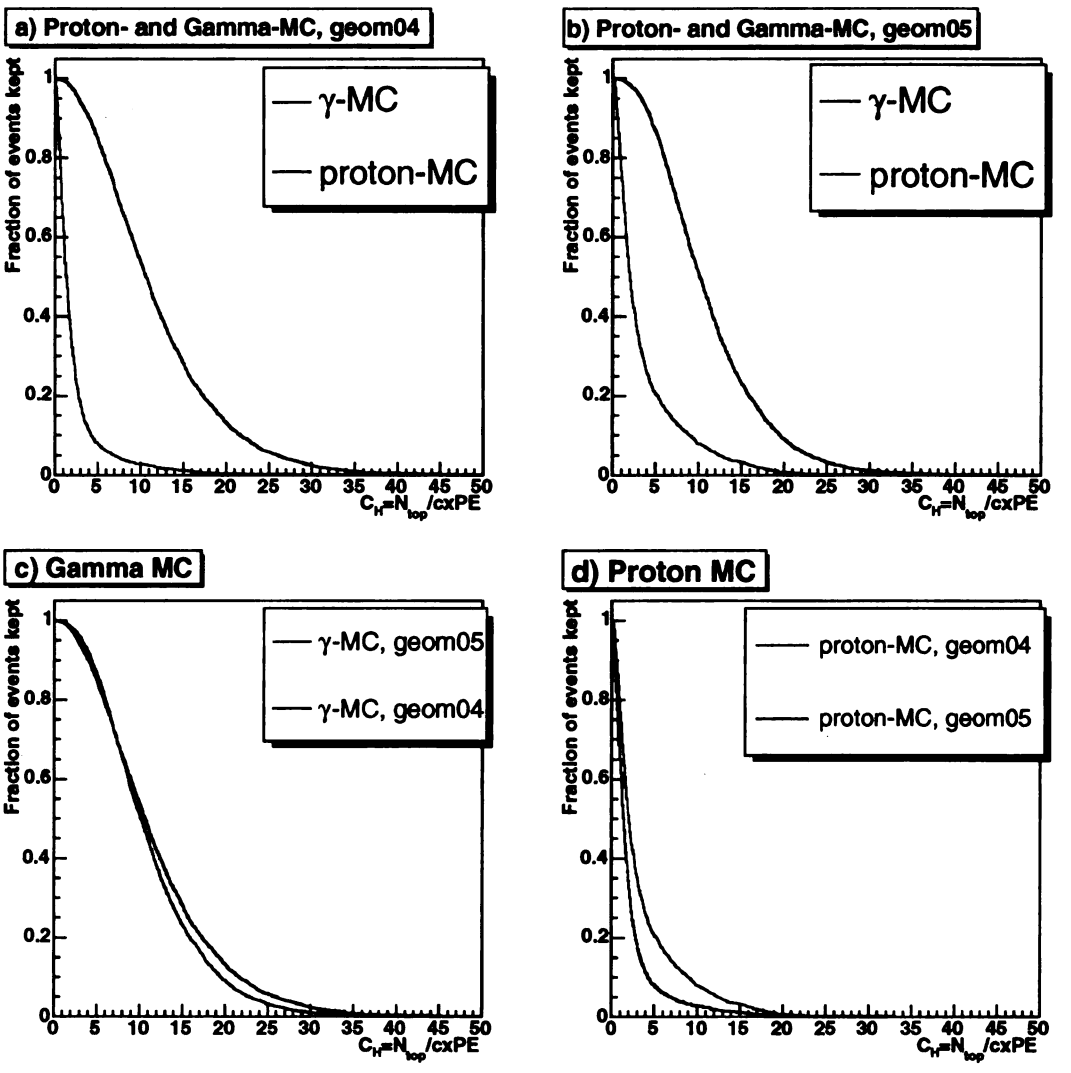

Figure 11: The efficiency distribution for both geometries in parameter-space: a) for geom04 and both primaries, b) for geom05 and both primaries, c) for gamma-MC and both geometries, d) for proton-MC and both geometries

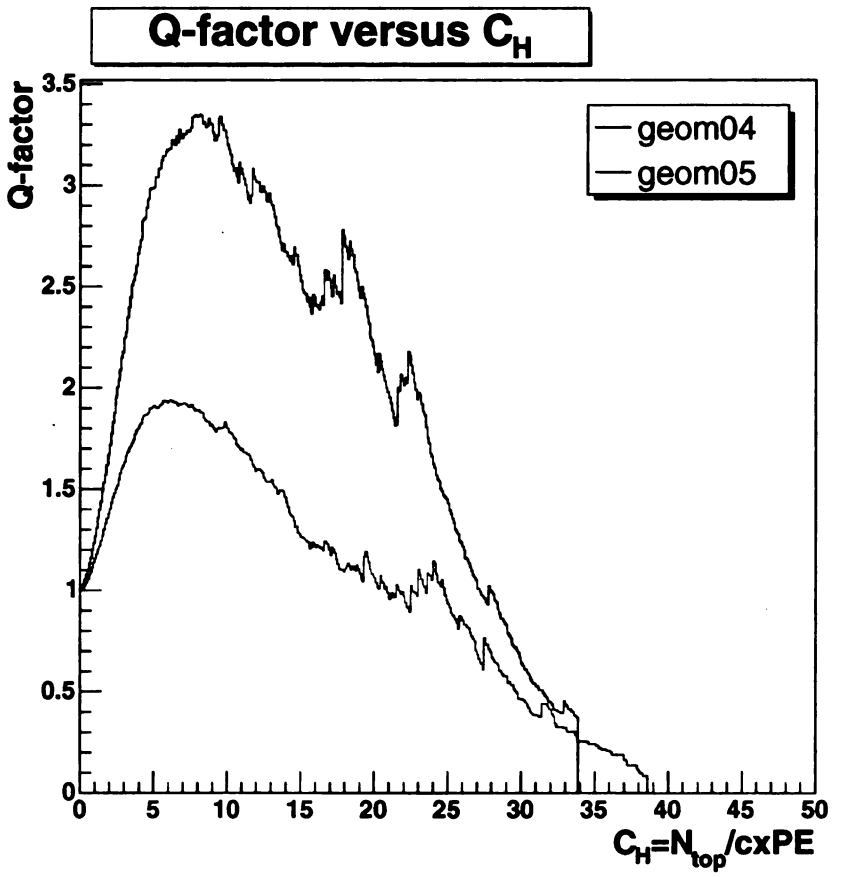

Figure 12: Q-factor versus C_H for both geometries

5.2.2 AX_3

The parameter AX_4 includes information about the outriggers. The HAWC geometries do not include such outriggers, the parameter AX_4 therefore cannot be applied to HAWC. However a slight modification which simply excludes the outrigger information can be used for HAWC. The new parameter AX_3 includes only the variables N_{top}, N_{fit} and $cxPE$, thus keeping AX_4's character as a variable that compares top to bottom layer and weights it with the fit information. AX_3 is defined as

$$AX_3 = \frac{N_{top} \cdot N_{fit}}{cxPE}. \tag{12}$$

In analogy to Milagro one and two dimensional cuts in AX_3 and CX_2 can be applied.

Figure 13 shows the normalized event-distribution for gamma and proton primaries for the two geometries in parameter space. The left side shows geom04, the right side shows geom05. For both geometries the proton events are confined to a relatively small area in parameter space compared to the γ events. Note that for both geometries there are a few proton events at relatively high values of CX_2 and AX_3.

Fig 14 shows the two-dimensional efficiency distribution. A point in this plot shows the fraction of events kept after a cut at the corresponding AX_3- and CX_2-values, keeping only events with AX_3 and CX_2 larger than the cut-values. For geom04 a fraction of less than 10% of the protons is at values $AX_3 > 2000$ and $CX_2 > 2$, for geom05 a comparable fraction of the protons in confined to the region $AX_3 > 3000$ and $CX_2 > 3$.

Figure 15 shows the two-dimensional Q-factor distribution for both geometries. The upper row shows a side view, the lower row the top view of the distribution. For geom04 Q-factors of more than 5 are possible, but only for very high values of

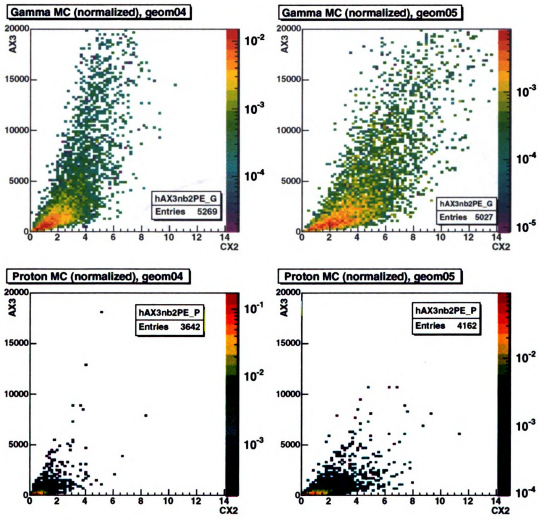

Figure 13: The normalized event distribution for both geometries in parameter-space, z-axis is logarithmic: a) γ-MC for geom04, b) γ-MC for geom05, c) proton-MC for geom04, d) proton-MC for geom05.

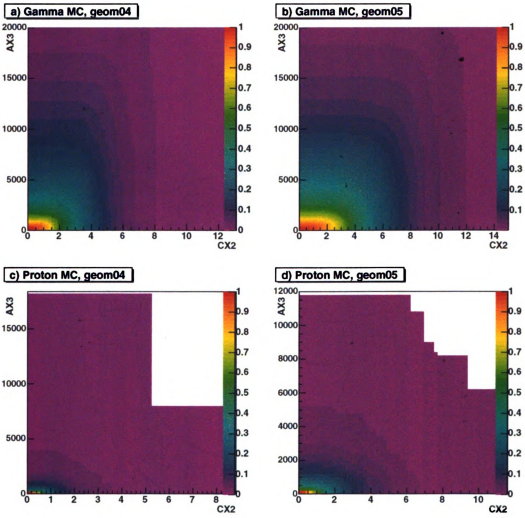

Figure 14: The efficiency-distribution for both geometries in parameter-space: a) γ-MC for geom04, b) γ-MC for geom05, c) proton-MC for geom04, d) proton-MC for geom05.

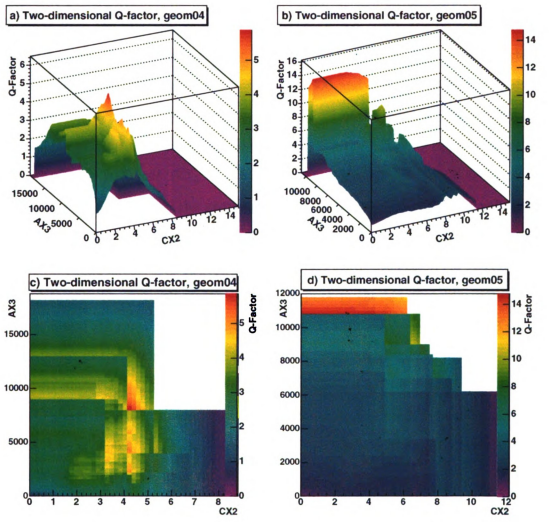

Figure 15: The Q-factor distribution for both geometries in parameter space: a) side view for geom04, b) side view for geom05, c) top view for geom04, d) top view for geom05.

AX_3 and CX_2 (a cut at $AX_3 = 8100$ and $CX_2 = 4.2$ e.g. leads to Q=5.5). As mentioned before for very high values of AX_3 and CX_2 we run out of proton-events, consequently the peaks in the Q-factor-distribution for high values of AX_3 and CX_2 have to be considered as statistical fluctuations. Safe values for the Q-factor can be obtained from the plateau-like structure for $CX_2 < 3.5$. Here the proton statistics should be sufficient. In the area $0 \leq AX_3 \leq 6000$ and $0 \leq CX_2 \leq 4$ Q-factors above 3 are achievable, e.g. a cut in $AX_3 = 4000$ and $CX_2 = 4$ leads to Q=3.4, while keeping about 12.3% of the gammas and 0.13% of the protons. The percentage of gammas passing this cut is very low, so that for the following analysis a softer cut at $AX_3 = 2000$ and $CX_2 = 2.5$ is chosen. This cut leads to a Q-factor of 3.2 while keeping 31.8% of the gammas and 1% of the protons. The cut values lie in the middle of a very smooth plateau, so that fluctuations due to the low proton statistic can be excluded. For geom05 there are very few proton-events at AX_3-values around 11000. These events cause the striking peak in the Q-factor distribution for $CX_2 < 6$ and $AX_3 \approx 11000$. Excluding the region with $AX_3 > 8000$ and $CX_2 > 7$ the Q-factor distribution is a broad plateau that, with growing AX_3 and CX_2, rises relatively smoothly. Q-factors above 3 can be achieved in the region $AX_3 > 3000$ and $CX_2 > 3$. In order to not decrease the percentage of gammas kept too much the values $AX_3 = 4000$ and $CX_2 = 5$ are chosen. Such a cut leads to a Q-factor of 4.07 while keeping 25% of the gammas and 0.4% of the protons.

As can be seen from figure 16 a one dimensional cut only in AX_3 leads to Q-factors not above 3 for geom04 and not above 4 for geom05. The peak around $AX_3 = 11000$ for geom05 corresponds to the peak in two-dimensional parameter-space described earlier. In order to exclude statistical variations a one-dimensional cut in AX_3 should be softer than 7000, thus leading to Q-factors between two and three for both geometries.

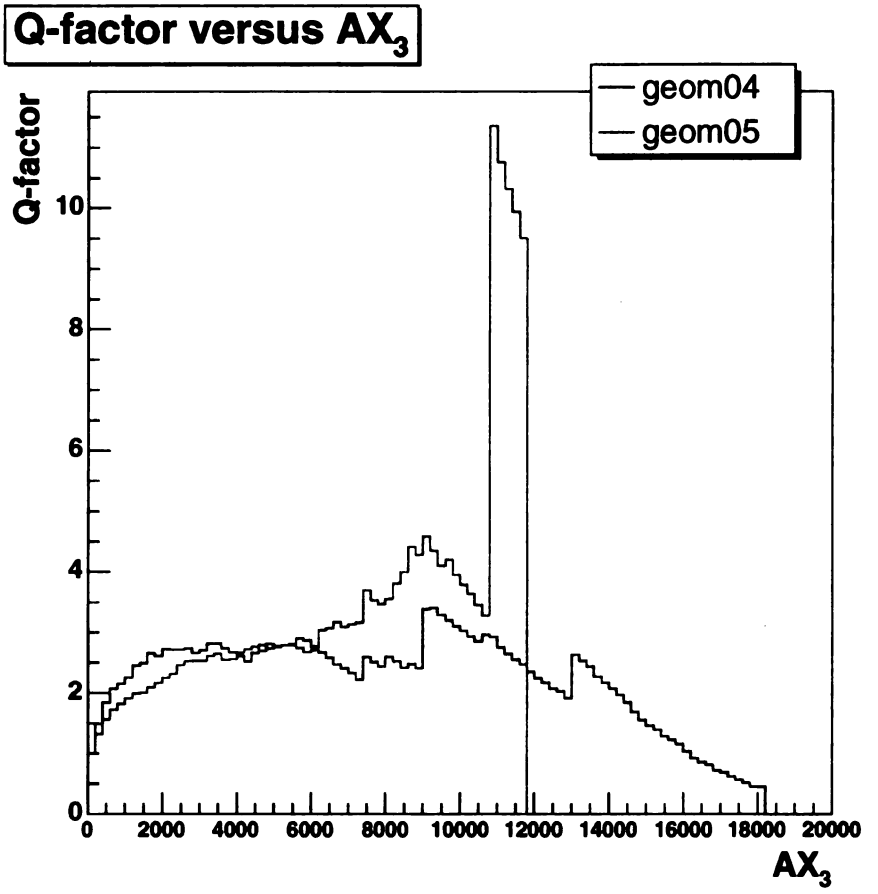

Figure 16: Q-factor versus AX_3 for both geometries.

5.2.3 Comparison and energy-spectrum

Since GRBs and steady sources like the Crab-nebula are some of the most interesting sources for HAWC it is necessary to look at the influence of these cuts on the energy-spectrum.

Geometry	AX_3	CX_2	Q-factor	C_H	Q
geom04	2000	2.5	3.2	8	3.3
geom05	4000	5	4.07	6.1	1.9

Table 3: The most successful cuts in both geometries.

Table 3 shows an overview over the most successful cuts in both geometries.

Figure 17 shows the fraction of triggered gamma and primaries as a function of energy that are retained after these cuts. A trigger condition of at least 55 tubes in the top layer are struck and at least 20 tubes are participating in the fit is applied. In addition to the cuts in AX_3, CX_2 and C_H the N_{fit}-cut of 20 and the corresponding cuts in Δ_{angle} have been applied. Without cuts in AX_3, CX_2 and C_H geom05 triggers more lower-energetic events compared to geom04. The median of the distribution for no γ/p-separation-cuts is at about $2 \cdot 10^2$ GeV for geom05 and at about $3 \cdot 10^2$ GeV for geom04. For both geometries the cuts in C_H have comparable effects: They reduce the number of triggered events in the low-energy part significantly more than in the high energy part, the medians are shifted to about $3 \cdot 10^2$ GeV for geom05 and about $4 \cdot 10^2$ GeV for geom04 after the cuts in C_H. With the softer C_H-cut for geom05 the total number of events thrown away is less than for geom04: about 65.5% of the events are kept after the C_H-cut in geom04 while about 78.4% of the events are kept after the cut in geom05. The comparably hard cuts in AX_3 and CX_2 reduce the number of events passing the cut even more significantly: about 36.6% are kept in geom04 and only 22.3% in geom05. As for C_H the cuts in these two variables reduce the number of lower-energetic events more than the number of higher-energetic events. The medians

are shifted to about $4 \cdot 10^2$ GeV for geom05 and about $5 \cdot 10^2$ GeV for geom04. For very high energies, above 2TeV the cuts in AX_3 and CX_2 and the C_H-cut perform similarly, i.e. they keep a similar fraction of events. For energies larger than 10TeV the AX_3 and CX_2-cut keeps more events then the C_H-cut for geom04.

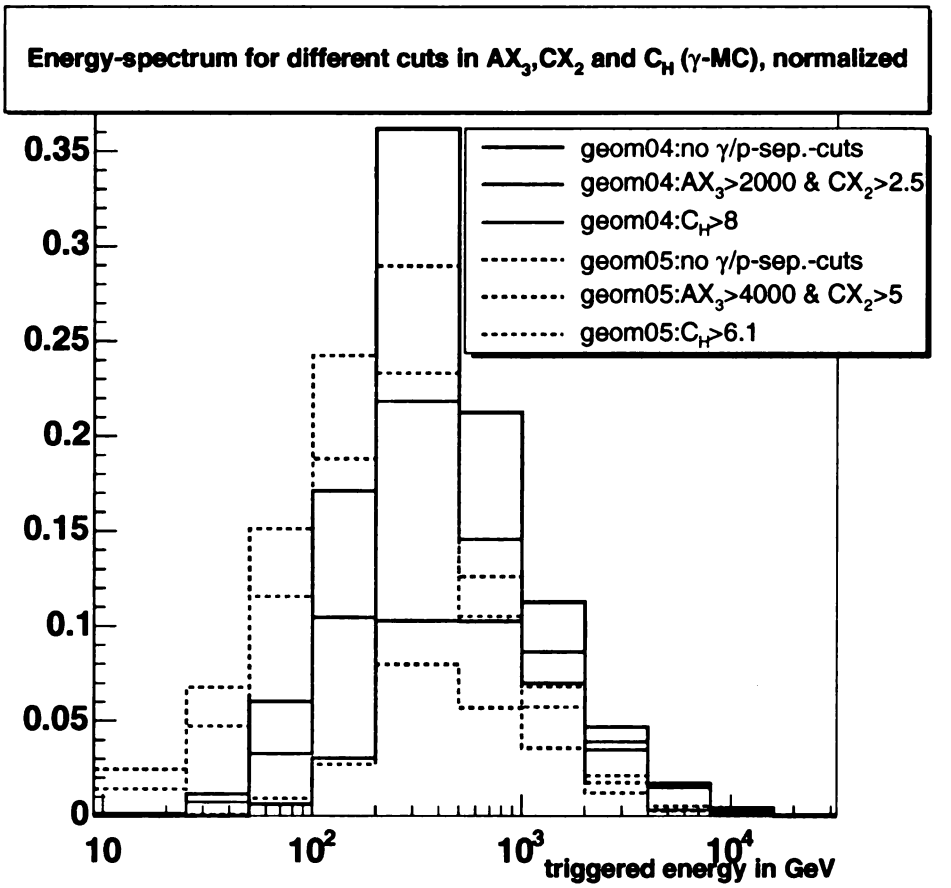

Figure 17: The triggered energy-spectrum without and with cuts, full lines: geom04, dotted lines: geom05. No γ/p-separation-cuts means that only cuts in bin size and N_{fit} are applied. For each geometry the spectra are normalized with respect to the case of no γ/p-separation-cuts.

6 Effective area

The effective area is the thrown area scaled by the fraction of events that are detected, therefore it can be interpreted as a measure for the detector's efficiency. The effective area A_{eff} is defined as

$$A_{eff} = \frac{N_{pass}}{N_{thrown}} \cdot A_{thrown}, \tag{13}$$

where N_{thrown} is the number of thrown events, A_{thrown} is the area over which the showers where thrown (normal to incident direction, $A_{thrown} = \pi \cdot 1km^2$, see section 2.2) and N_{pass} is a number of events that are successfully reconstructed and pass certain cuts (see section 5).

Figure 18 shows the effective area as a function of primary energy for different cuts in AX_3 and CX_2 as well as C_H. Only events that fulfill the following conditions are considered in N_{pass}:

-at least 55 tubes in the top-layer are struck and at least 20 tubes are participating in the fit (trigger-condition)
-cuts in Δ_{angle} according to the optimal values for each geometry (see table 2)
-additional cuts in AX_3, CX_2 or C_H as indicated

In the following the term "no γ/proton-separation-cuts" is used in order to express that the trigger condition is fulfilled and that for gamma primaries the corresponding Δ_{angle} cut is applied. No further cuts in AX_3 and CX_2 or C_H are applied.

The effective area increases for both geometries up to about $2 \cdot 10^4 m^2$-$10^5 m^2$ at 1TeV. From 1TeV to 10TeV the effective area is essentially constant and starts dropping around 10TeV. Without γ/p-separation-cuts the effective area at low energies is significantly larger for geom05 than for geom04. With rising energy the effective area for geom04 grows faster than for geom05, so that geom04 reaches an effective area of $5 \cdot 10^4 m^2$ at an energy of 3 TeV and geom05 reaches $7 \cdot 10^4 m^2$ at 1.5 TeV. In figure

18 this effect is stressed by the logarithmic scale on the y-axis. The decrease of the effective area due to cuts in AX_3 and CX_2 is more drastic for lower-energetic events for both geometries.

As discussed in section 5.2.3 the cuts in AX_3 and CX_2 reduce the number of lower-energy events more significantly than the number of higher energetic events.

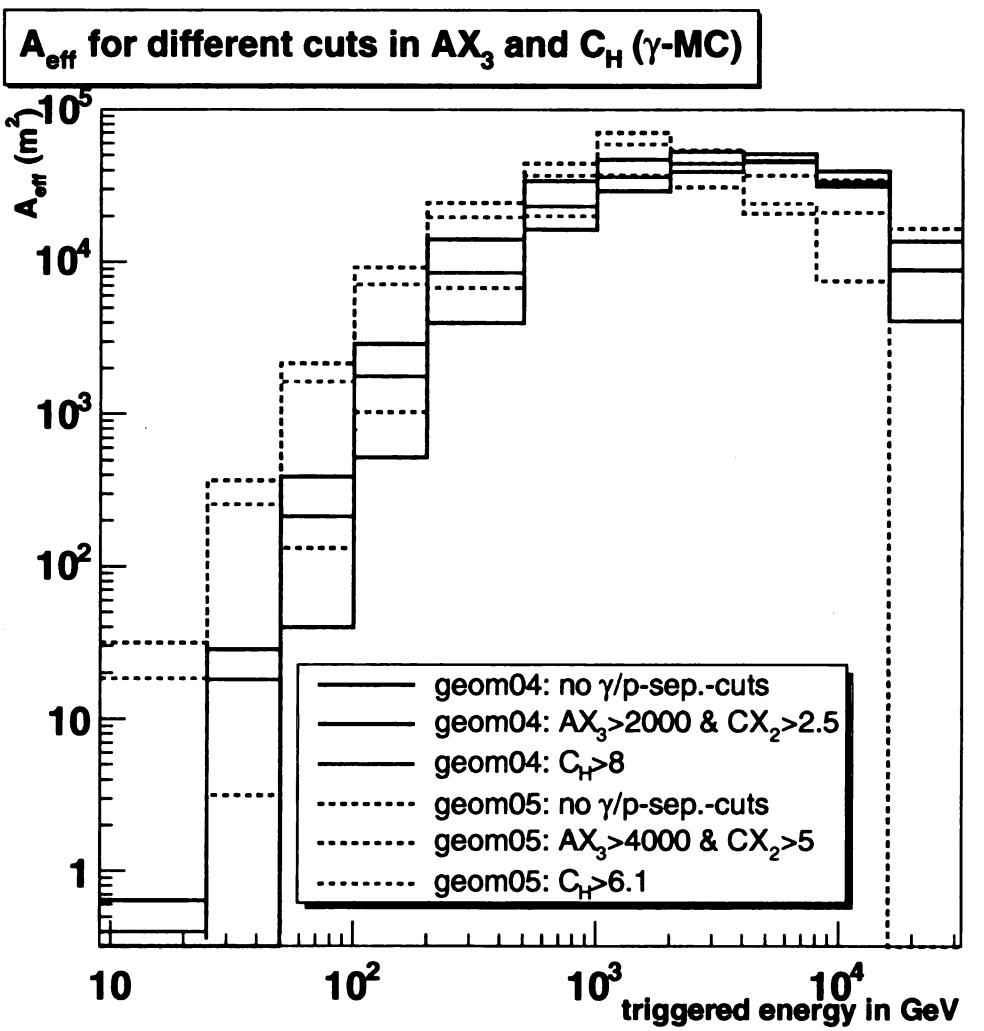

Figure 18: Effective area for both geometries and the most successful cuts given in table 1, geom04: full lines, geom05: dotted lines.

For geom05 these cuts also throw away a large portion of the higher-energetic events, while for geom04 the AX_3 and CX_2 cuts perform even better than the softer C_H cut. The C_H cut reduces the effective area of geom04 in a similar way the softer C_H cut of geom05 does it. At energies larger than 2TeV the decrease in effective area due to the C_H-cut in geom04 is less drastic than the decrease due to the softer cut in geom05.

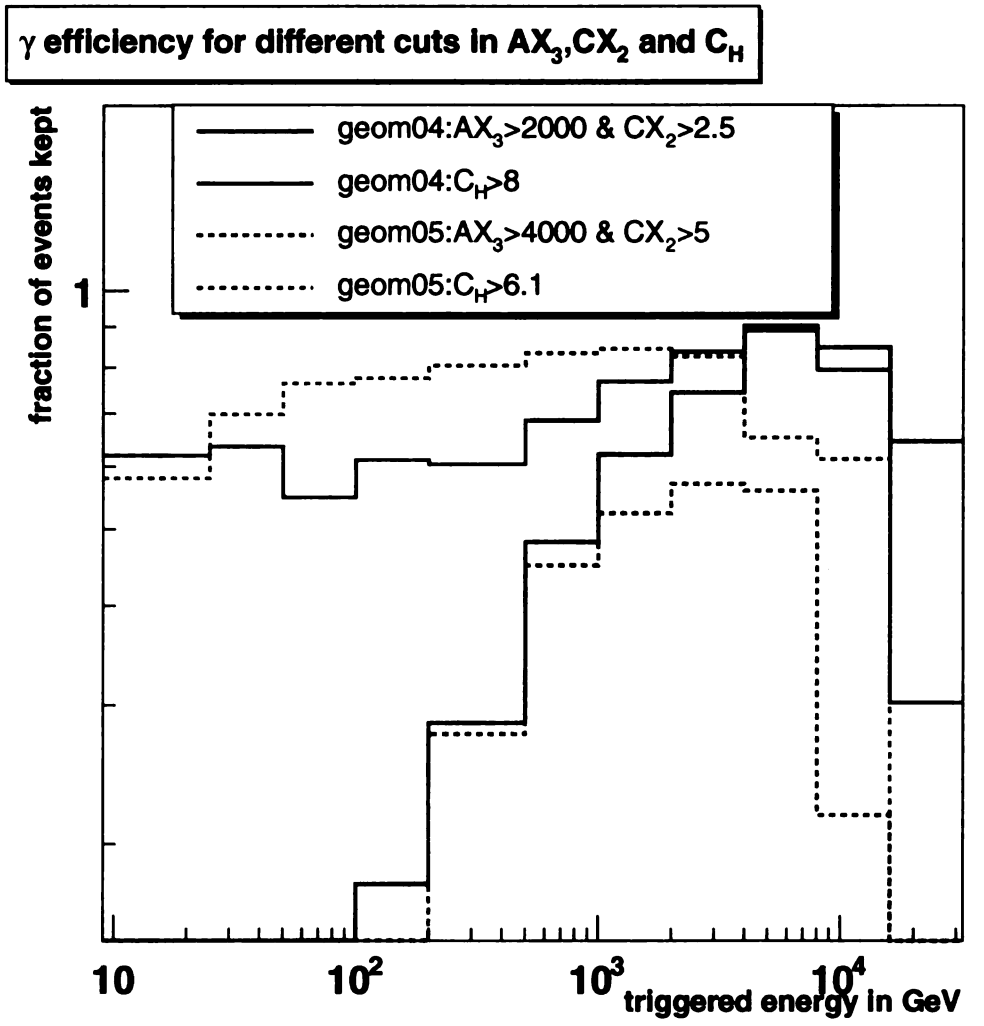

Figure 19: γ efficiency for the most successful γ/p-separation cuts.

Figure 19 shows the γ efficiency for the most successful γ/p-separation cuts. The ratio of the number of γ events that pass the γ/p-separation cuts in addition to the cuts in N_{fit} and bin size and the number of γ events that pass only the cuts in N_{fit} and bin size is plotted on the y-axis. For both geometries the cuts in AX_3 and CX_2 reduce the number of low energy events significantly more than the number of high energy events. The reduction of high energy events is more drastically for geom05.

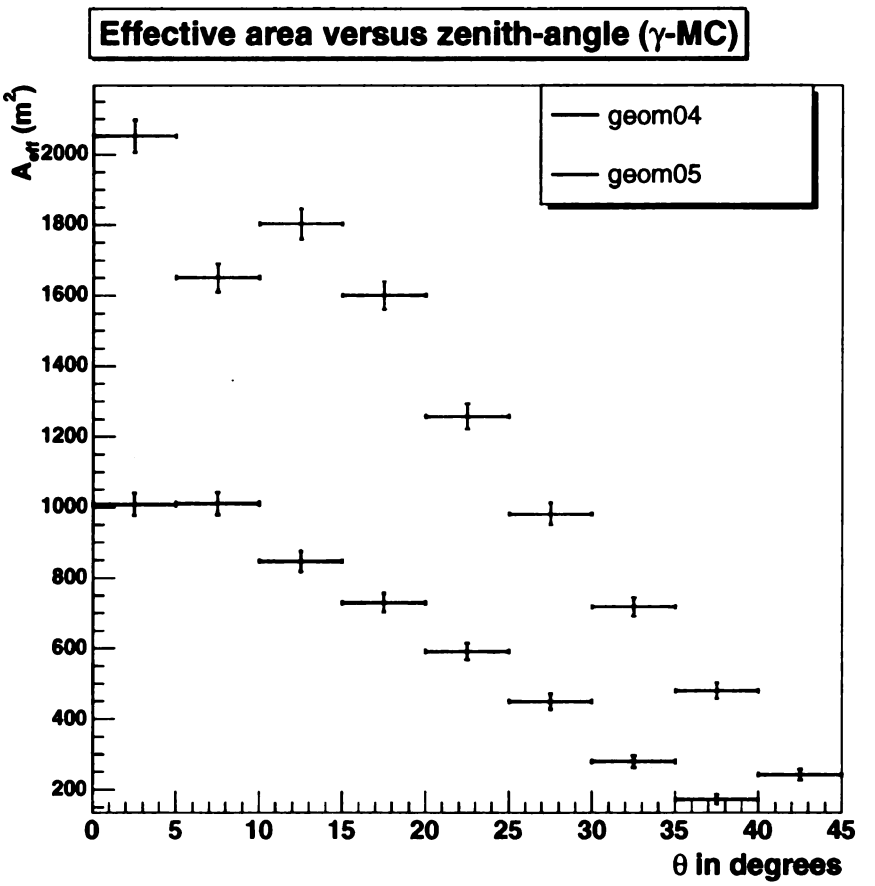

Figure 20: Effective area versus zenith angle. Only cuts in bin size and N_{fit} are applied.

This is in agreement with the behavior of the effective area at high energies for this cut. At energies larger than 2TeV the decrease in effective area due to this cut

is more significant for geom05 than geom04. The C_H cut reduces the number of low energetic events more drastically for geom04 than for geom05. At energies above 2TeV, however, this cut keeps a larger fraction of events for geom04 than for geom05, thus leading to the stronger decrease in effective area in this energy range for geom05.

The effective area and therefore the sensitivity of HAWC is strongly dependent on the zenith angle. This is because the area normal to the shower front is maximal for the zenith.

The zenith angle dependence of the effective area for gamma-ray showers thrown over the complete energy range from 10 GeV to 100 TeV is shown in figure 20. In this figure the effective area is defined as $A_{eff}(theta) = \frac{N_{pass}(\theta)}{N_{thrown}(\theta)} \cdot A_{thrwon}$. $N_{pass}(\theta)$ is the number of events in the corresponding zenith angle range ($\Delta\theta = 5$) that pass the cuts in N_{fit} and bin size and $N_{thrown}(theta)$ is the number of thrown events in the same zenith angle range. No γ/p-separation cuts are applied. $A_{eff}(\theta)$ can be interpreted as the effective area the detector would achieve if the complete overhead sky was "empty" and only a ring centered on the zenith with width $\theta = 5$ for each zenith angle range would include sources. Since events out of the complete thrown energy range are taken into account the used energy bin can be considered infinite. One can see that, as expected, HAWC is most sensitive to showers close to the zenith. The effective area obtained at the zenith with geom05 is nearly the double of the effective area expected from geom04. This is consistent with the energy-dependence of the effective area, where similar ratios between the effective areas of the two geometries are predicted (see figure 18). For geom04 and zenith angles smaller than 10^o the effective area is approximately constant, afterwards the effective area drops drastically. For geom05 the effective area also decreases at zenith angles higher than 10^o, the low entry for $5^o < \theta < 10^o$ is assumed to statistical fluctuation due to the low number of events that are expected from low zenith angles (the events are thrown isotropically over the entire field of view). The factor of two between the effective areas of the two

geometries stays approximately constant over the entire zenith-angle-range.

7 Sensitivity to point sources

The Crab nebula is a remnant that resulted from a supernova explosion about 900 years ago. It is located in the constellation of Taurus, at 22^o 01' declination and 05h 34.5min right ascension (position of the Crab nebula in the year 2000), at a distance of 6000 light years. Observed for nearly a millennium (with a big gap between the year 1054 and the first observations with the help of telescopes) it is the best studied source in the cosmos at all wavelengths. The Crab nebula was one of the first radio-sources detected, it is one of the strongest x-ray sources and it was the first supernova remnant to be clearly identified with a pulsar. It also was one of the first gamma-ray sources detected (from balloon borne experiments [12]). The Crab-pulsar is a fast radio pulsar (33ms), at many wavelengths the emission from the pulsar dominates the nebular emission. At optical wavelengths the nebular emission is a complex superposition of different phenomena (see figure 21).

The Crab nebula was the prototype source for synchrotron radiation by cosmic electrons and for Compton-synchrotron emission from cosmic sources [28],[19]. In the volume near the pulsar the emission is variable on timescales of days, but it can be generally treated as a steady source. The first satellite-borne spark-chamber telescope SAS 2, which measured its energy spectrum from 30 MeV to 500 MeV, established it as a high energy source. Later a steady component in addition to the pulsed component has been identified by the COS-B experiment. Up to 500MeV this steady component could be fitted by a power law of spectral index -2.7+-0.3 (while the pulsed component lead to an index of -2.00+-0.10). An extrapolation of these spectra to very high energies indicated that it would be unlikely the soft steady signal would be detectable whereas the hard pulsar spectrum looked promising if the spectrum did not cutoff above 10 GeV. Assuming that the radiation from radio to x-rays from the nebula is due to synchrotron radiation by relativistic electrons, then the

same electrons should Compton scatter the photons, thus boosting them to gamma ray energies [19].

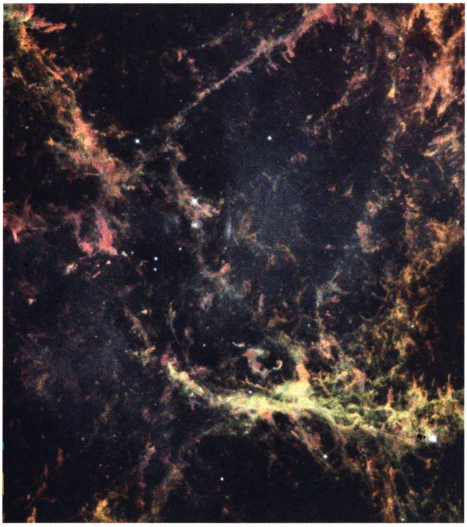

Figure 21: A view into the center of the Crab-Nebula (Figure:STScI/NASA).

The resulting gamma-ray spectrum would be most easily detectable at 100-1000GeV energies, dipping sharply thereafter, because the Klein-Nishina cross section has to be taken into account. Later the COMPTEL and EGRET observations of the Crab indicate variability between 1 and 150 MeV [13]. At higher energies, however, EGRET

shows no evidence for variability. The EGRET observations cover the synchrotron and Compton parts of the spectrum. The gamma rays up to 300MeV are synchrotron radiation; unlike the rest of the spectrum they may exhibit some variability at this upper end of the spectrum corresponding to the highest energy electrons in the nebula. In the TeV range there is no evidence for any significant variation. The Compton-synchrotron model does not predict short term variations although there might be a long term secular decline [30]. In the 300 GeV to 3 TeV range, the Crab Nebula is now considered a standard VHE candle. It has been detected by eight ground based gamma-ray telescopes using a variety of techniques. The spectrum of the Crab Nebula stretches from photons of energies less than 10^{-4}eV to photons of nearly 10^{14} eV.

As said before the lower part of the photon energy spectrum (up to 100MeV) is explained as synchrotron emission from relativistic electrons (energies as high as 10^{15})within the nebula. The electron acceleration is assumed to occur within the termination shock of the pulsar wind, at a distance of 0.1 pc from the pulsar ($\sim$ 12 arcsec)[25]. From there on the electrons diffuse into the nebula. The presence of such high energy electrons in the presence of the luminous nebula inevitably leads to a Compton-scattered gamma-ray spectrum that extend to very high energies [19]. The lower energetic target photons can be either synchrotron photons, the 2.7K background or thermal radiation from dust. In the VHE energy gamma-ray bands the scattering is in the Klein-Nishina-range with electrons having energy from 2-30 TeV and the soft photons having energies from $5 \cdot 10^{-3}$ to 0.3 eV.

7.1 Crab-like sources

The sensitivity of different HAWC-geometries for the Crab-nebula and Crab-like sources is of special interest. Using a spectrum with a spectral index of -2.49 for

gammas and -2.7 for protons and a flux of $3.2 \cdot 10^{-7} m^{-2} TeV^{-1} sec^{-1}$at 1 TeV the transit of the source through HAWC's field of view for a chosen day has been simulated and the number of protons and gammas that HAWC is expected to see during this transit has been calculated. Since the actual event rate for HAWC and therefore the link between MC and data is unknown, Milagro's event rate is used in order to scale the results: The scaling-factor k is defined as

$$k(\delta) = \frac{n_{(p,milagro-data)}(\delta)}{n_{(p,milagro-MC)}(\delta)}, \tag{14}$$

where $n_{(p,milagro-data)}(\delta)$ is the number of protons for Milagro-Data we expect per day from the Crab and $n_{(p,milagro-MC)}(\delta)$ is the number of protons for Milagro-MC we expect per day and declination δ from a Crab-like source. The factor k therefore can be considered as an event rate that tells us how many data events per Monte Carlo event we can expect from the source. A 5σ-significance of the Crab corresponds to: $5\sigma = 5 \cdot \sqrt{n_p \cdot k}$. In order to express the sensitivity of a detector geometry with respect to Milagro's sensitivity to the Crab-nebula we can define the unit Crab: The number of signal events necessary for a 5σ-significance is: $N_s = 5 \cdot \sqrt{n_p \cdot k}$. The number of events detected from the Crab is N_{Crab}. Therefore the number of signal events in Crab units is :

$$\frac{N_s}{N_{Crab}} = \frac{5 \cdot \sqrt{n_p \cdot k}}{N_{Crab}}. \tag{15}$$

Thus, the sensitivity in Crab expresses the fraction of Crab-flux needed to observe the Crab-nebula at the 5σ-level. To calculate the sensitivity in millicrab (mCrab) per declination we need the four values $n_{(\gamma,hawc)}$, $n_{(proton,hawc)}$, $n_{(p,milagro-MC)}$ and $n_{(proton,milagro-data)}$ per declination. For the Monte Carlo data these values are easily obtained by simulating the source transit as described above. For the real Milagro data the results given in [6] have been used: during the 1185 days of observation a background of 18,365,694 events has been estimated. This leads to an average number

of 15498.48 protons per day from the Crab. In addition we have to take into account that the Milagro data refer to a larger bin size of 1.2. Assuming a flat background spectrum we can scale the number of protons to the bin sizes of the two HAWC geometries. With

$$N_p(r) = N_p^0 \cdot r^2, \tag{16}$$

where $N_p(r)$ is the number of protons in a bin with radius r and N_p^0 is the number of protons in a bin with radius 1, we can estimate the number of protons from the Crab-nebula Milagro would have detected with a differen bin size through

$$N_p(r_{HAWC}) = N_p(1.2) \cdot \frac{r_{HAWC}^2}{1.2^2}, \tag{17}$$

where r_{HAWC} is the optimal bin size for each geometry. For a Crab-like source at a different declination we expect a different number of protons per day. In order to implement the declination dependence a sub-run of Milagro data with a duration of a few minutes has been taken and the number of protons in each declination bin has been counted. Dividing the resulting histogram by the number of events from the Crab's declination and multiplying it with the average number of events Milagro would have detected from the Crab per day if the optimal bin sizes for the two HAWC geometries would have been used gives an estimate of the declination dependence.

The results are presented in figure 22 to 26. Figure 22 shows the number of protons and gammas we expect from the Crab in a single transit for both geometries. Figure 23 shows the declination dependence of the scaling factors k for the two geometries. Note that the difference between the scaling factors is a result of the different bin sizes used and therefore purely geometric. Figure 24 finally shows the sensitivity of the two HAWC geometries for a Crab-like source for different γ/p-separation-cuts at different declinations. Since the effective area of HAWC strongly depends on the zenith angle (see figure20) HAWC is most sensitive for overhead sources with declinations between

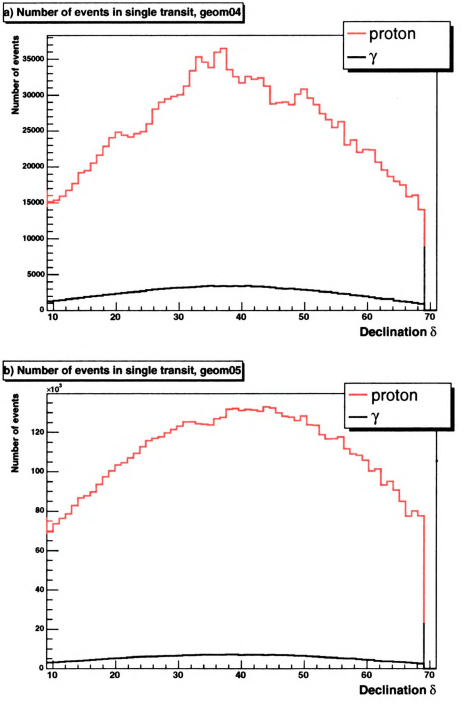

Figure 22: Number of events expected from the Crab-Nebula per day and declination for HAWC-MC. a) geom04, b) geom05.

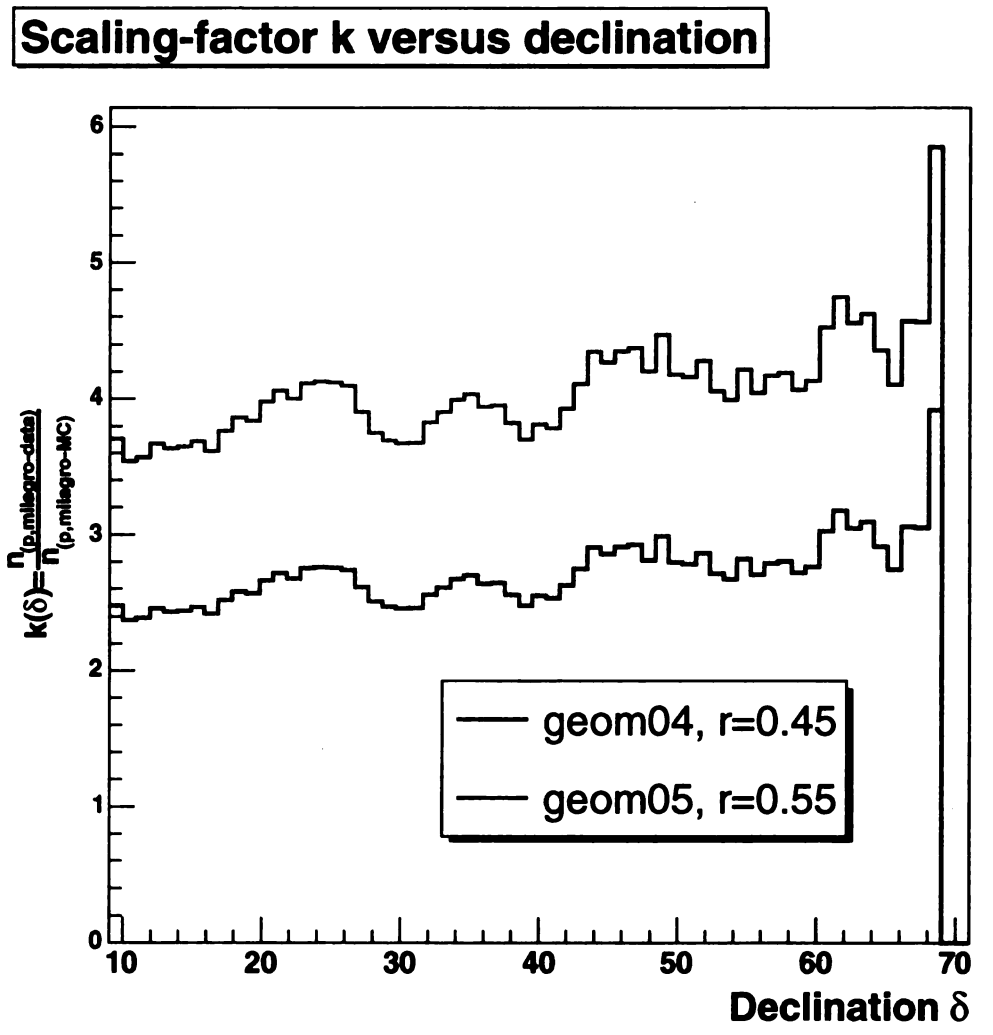

Figure 23: The scaling-factor k.

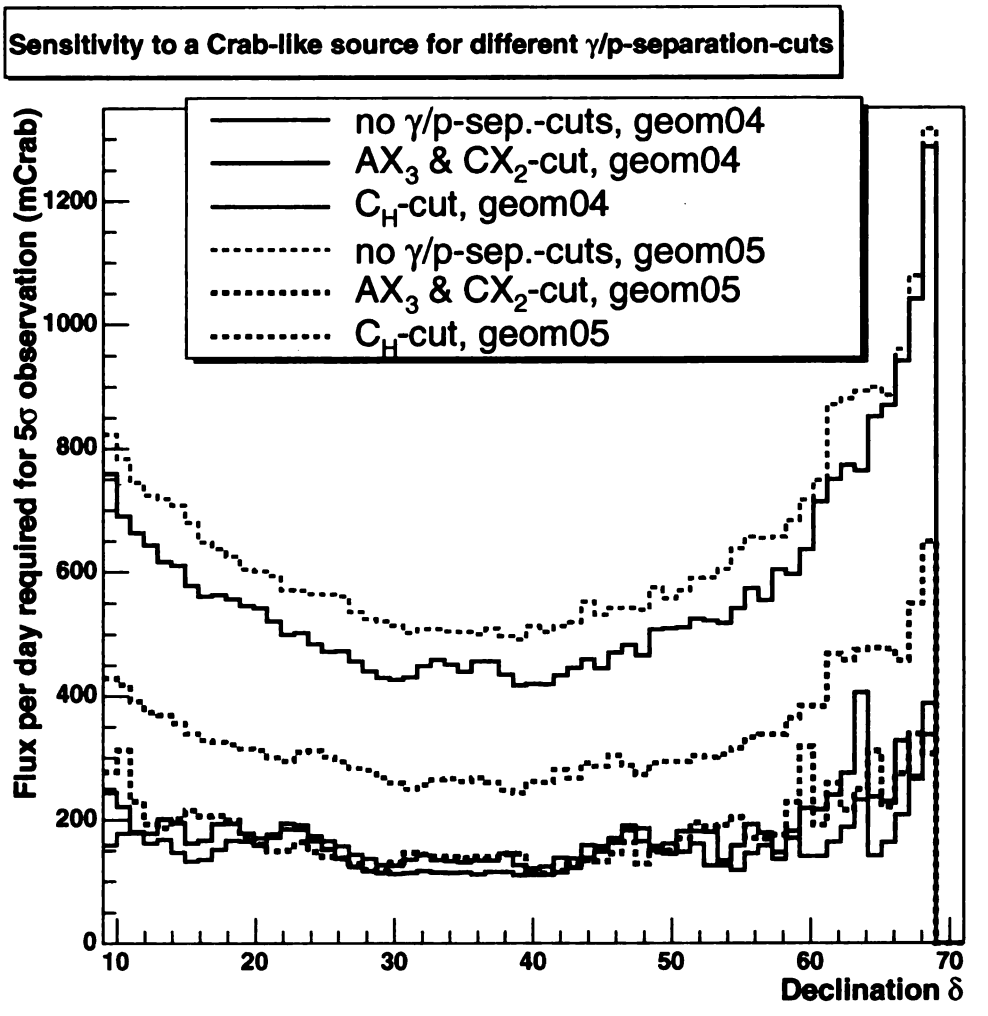

Figure 24: Sensitivity of both geometries for a Crab-like source versus declination for the most successful cuts in AX_3, CX_2 and C_H.

30^o and 40^o.

Without γ/p-separation-cuts sensitivities of about 450mCrab per day can be achieved for overhead sources with geom04 and sensitivities of about 500mCrab per day with geom05.

Despite the higher effective area of geom05 the smaller bin size of geom04 leads

to slightly higher sensitivities. The sensitivity for the Crab-nebula is 0.5 Crab per day for geom04 and 0.58 Crab per day for geom05. For both geometries the AX_3 and CX_2 cut increases the sensitivity by a factor of more than 3. For geom04 the hard C_H cut leads to nearly the same gain in sensitivity and the softer C_H cut in geom05 still leads to an increase in sensitivity by a factor of about 1.5. With AX_3 and CX_2 cut the sensitivity for the Crab-nebula is 0.2 Crab per day for geom04 and 0.15 Crab per day for geom05. The C_H-cut leads to sensitivities of about 0.19 Crab per day for geom04 and about 0.3 Crab per day for geom05.

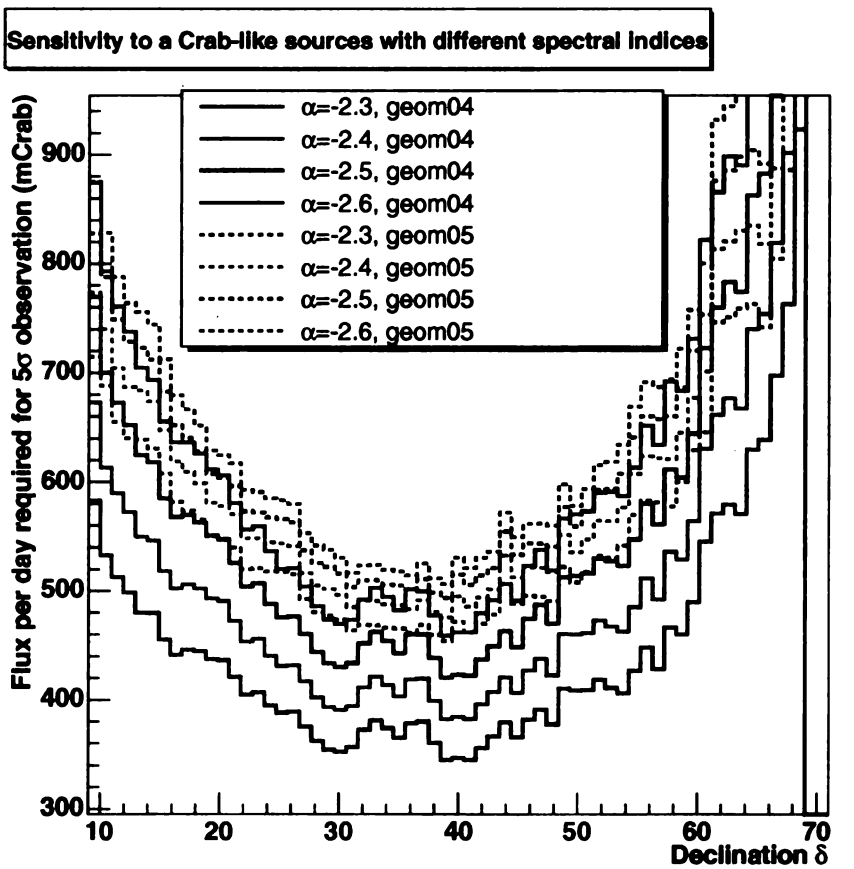

Figure 25: Sensitivity of both geometries for a source similar to the Crab-nebula versus declination for different spectral indices.

In order to examine the sensitivity of the two HAWC geometries to sources similar to the Crab, but with a slightly different spectral index, the sensitivity of the two HAWC geometries for sources with the flux and right ascension of the Crab-nebula, but different spectral indices has been calculated for different declinations.

Figure 25 shows the sensitivity of the two HAWC geometries for spectral indices α in the range -2.3 to -2.6. For all spectral indices higher sensitivities are achieved with geom04. For spectra harder than the spectrum of the Crab-nebula (-2.49) the difference between the sensitivities of the two geometries becomes less dramatic. A harder spectrum leads to an overall higher sensitivity because of the higher effective area for higher energies. Reducing the spectral index by 0.1 leads to a decrease in sensitivity by about 50mCrab for an overhead source in geom04 and about 25mCrab in geom05. While the improvement in sensitivity due to a harder spectrum is approximately constant for geom04, the improvement in sensitivity seems to grow for geom05. Increasing the spectral index from -2.6 to -2.5 leads to an increase in sensitivity by about 20mCrab and increasing it from -2.4 to -2.3 leads to an increase in sensitivity by nearly 30mCrab. For geom05 the increase in sensitivity due to a harder spectrum is for the steepest spectra not as drastic as for the flatter spectra. A higher sensitivity for a steep spectrum (< -2.4) can be expected if the effective area at low energies is larger, as the case for geom05 and energies lower than 2TeV. For this geometry a variation of the spectral index in the soft range does not affect the sensitivity as much as for geom04 where the effective area at low energies is smaller.

An overhead source with a spectral index in the range of -2.3 to -2.6 leads to 0.47 to 0.53 Crab per day with geom05 and 0.37 to 0.5 Crab per day with geom04.

The energy range over which the Crab spectrum has been taken into account is the complete range over which the Monte Carlo has been thrown (i.e. from 10 GeV to 100 TeV). Another interesting question is the sensitivity for Crab-like sources with

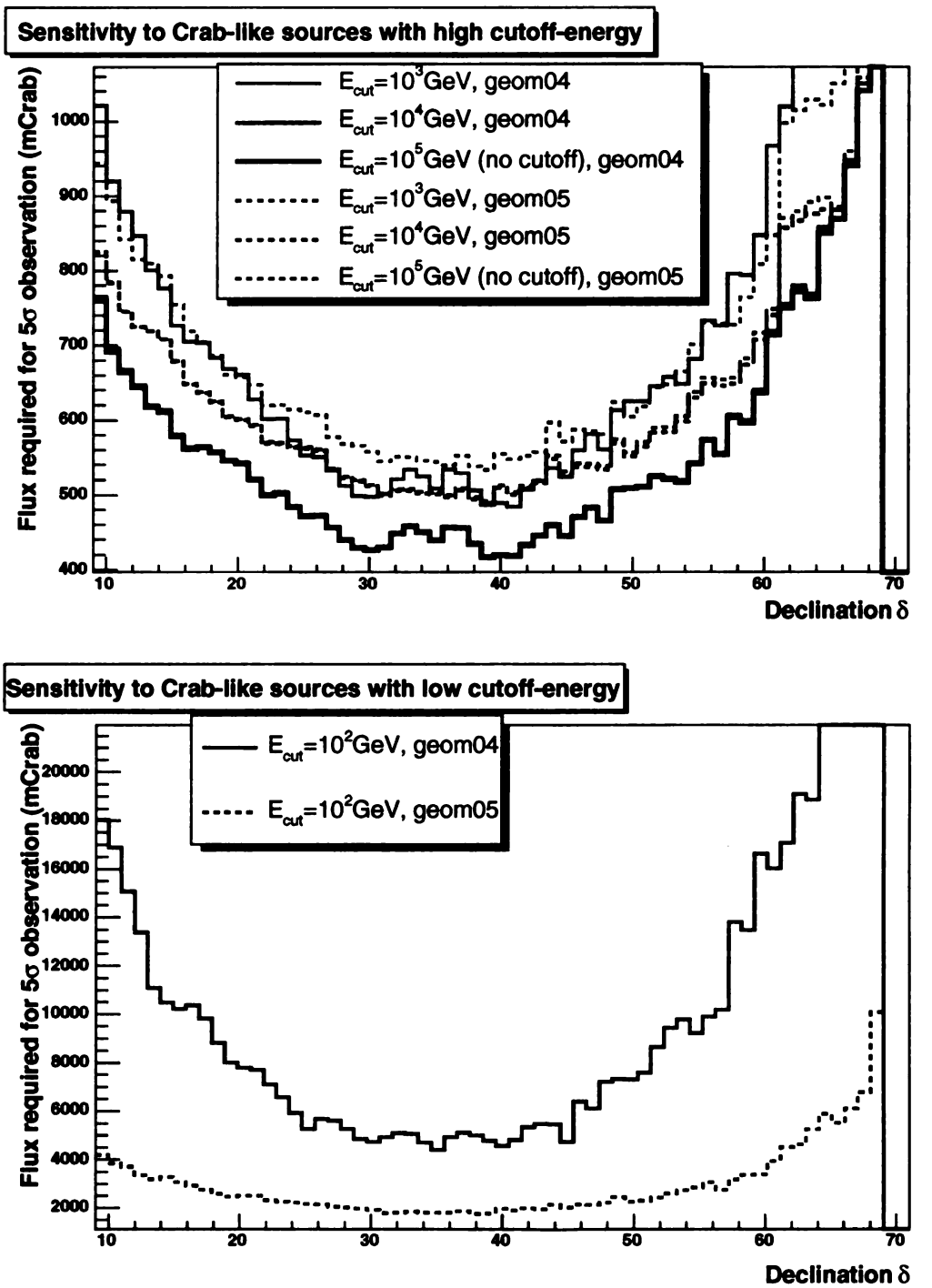

Figure 26: Sensitivity of both geometries for a Crab-like source versus declination for different cutoff-energies. Geom04: full lines, geom05: dotted lines.

a fixed spectral index but different energy cutoffs for the maximum energies.

Figure 26 shows the sensitivity versus declination at a fixed spectral index of -2.49 for three different cutoff-energies E_{cut}= 100GeV, 1TeV and 10TeV. The lowest E_{cut} is close to HAWC's simulated energy threshold of 10GeV so that only a small number of events can be detected from these sources. In addition the effective area for energies lower than 10GeV is comparably small (see figure 18). The expected sensitivities for overhead sources are in the range of 5.5Crab per day for geom04 and 2.1Crab per day for geom05. Since a steep spectrum with spectral index -2.49 is assumed, the fraction of events between 1TeV and 10TeV is small compared to the fraction of events between 10GeV and 1TeV. Since the effective area is nearly constant for both geometries in this energy range, the gain in sensitivity due to a cutoff at 10TeV compared to a cutoff at 1 TeV is therefore not as drastic as the gain due to a 1 TeV cutoff compared to a 100 GeV cutoff. The sensitivity for overhead sources with a spectral cutoffs between 1 TeV and 10 TeV is between 0.41 and 0.5Crab per day for geom04 and between 0.5 and 0.55Crab per day for geom05. The gain in sensitivity due to a higher cutoff energy at 10 TeV compared to a cutoff at 1 TeV is more significant for geom04 than for geom05 and higher overall sensitivities are achieved with geom04. Cutoff energies above 10 TeV do not lead to a significant increase in sensitivity. The increase in sensitivity due to a cutoff at 100 TeV compared to 10 TeV (i.e. the cutoff is invisible to the simulated detector-geometries, since only primaries out of the range 10 GeV to 100 TeV are thrown) is negligible for both geometries. As can be seen from figure 18 the effective area even drops in this energy range.

7.2 Gamma-Ray-Bursts

As described in the introduction, one of the main physics goals of HAWC is the detection of Gamma-Ray-Bursts. GRBs are the most luminous emissions in the universe

at any wavelength band observed so far. GRBs are assumed to be at cosmological distances, therefore they offer a new tool for the exploration of objects at the edge of the observable universe.

The GRB phenomenon is usually associated with energies between 50keV and 1MeV (hard x-rays to low energy gamma-rays), but results from the Solar Maximum Mission (SMM) and the EGRET detector on the Compton Gamma Ray Observatory suggest that there is a component at high energies.

The duration of a GRB is 10ms to 100s, they are observed at a rate of 1/day. It is possible to consider the radiation that constitutes the GRB without fully determining the central engine. The current model includes a relativistic fireball that originates from an event like [30]

(1) the merging of two neutron stars to form a black hole
(2) the core collapse of a massive star (more than ten solar masses, a so-called hypernova)
(3) the collapse of a neutron star into a hole formed in a supernova explosion (a so-called supranova)

Distances to over 20 GRBs have been measured, thus allowing an energy-estimate: For these 20 GRBs the total energy lies within $5 \cdot 10^{51}$ to $3 \cdot 10^{54}$ erg [30]. No other known astrophysical phenomenon emits a comparable amount of energy apart from the Big Bang.

GRBs have been observed with a duration from milliseconds to seconds. The pulse shapes show no correlation between different GRBs, but attempts have been made to subdivide the bursts according to their duration.

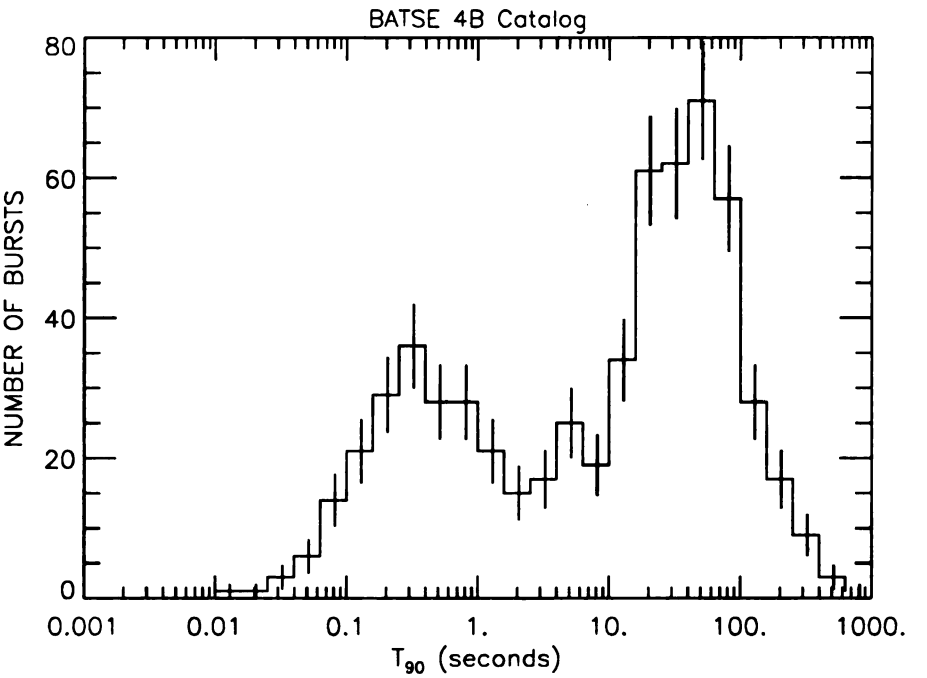

Figure 27: Time duration distribution as recorded by BATSE. The duration used here is T_{90} which is the interval time between the points in which the GRB has emitted 5% and 95% of its energy. Taken from [7].

Figure 27 shows the duration of GRBs. There is evidence for two classes of bursts with a break at t=2s.

The spectra show no spectral lines and are in general a smooth continuum with most of the power emitted at energies larger than 50 keV. The spectra can be modelled by two power laws with a differential index between 0 and -1.5 up to the power maximum and -2 to -2.5 after that (see figure 28).

The distribution of GRBs over the sky seems to be completely isotropic. BATSE detected more than 2700 GRBs with an angular resolution of a few degrees, see figure 29. There is no evidence for clustering, or repeated bursts and no correlation with any known class of cosmic objects.

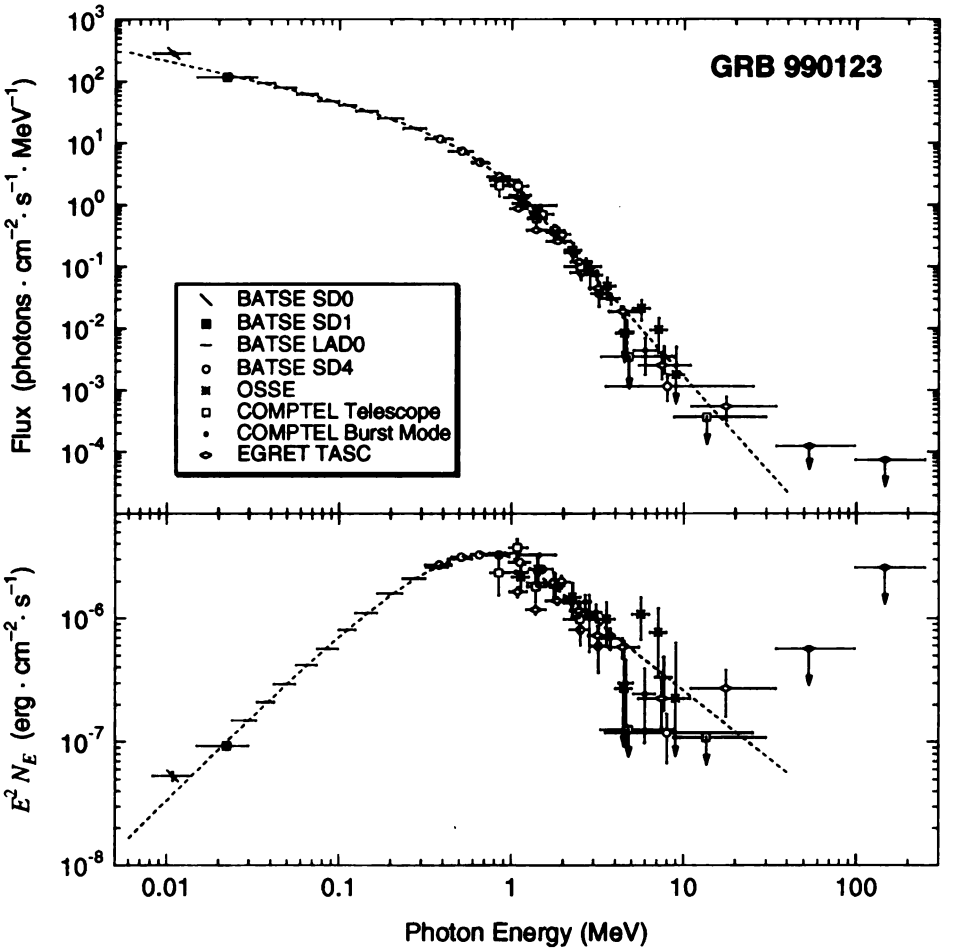

Figure 28: Complete spectrum of GRB990123 as measured by BATSE, OSSE, COMPTEL and EGRET on CGRO. Taken from [11].

In order to estimate the sensitivity of the HAWC detector for Gamma-Ray-Bursts the following logic is applied: The short duration of the burst allows a model that treats the source as a non-moving object that occurs at a certain point in the sky, characterized by azimuth and zenith angle. Since the effective area of the HAWC detector does not depend on the azimuth angle, only the zenith angle is of interest for the analysis. Assuming an isotropic GRB distribution over the sky one can tile the sky with angular bins and fill each bin with a fixed exposure, thus assuming an equal

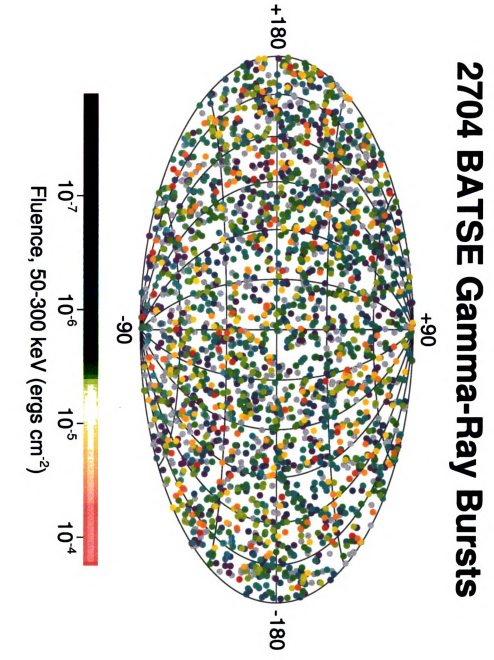

Figure 29: Distribution of the arrival directions of the 2074 GRBs detected by BATSE in galactic coordinates. Taken from [7].

probability for a GRB to occur in one of these bins. For this analysis an exposure of 60s has been chosen. A spectrum with spectral index of -2.0 models the source and a flux of $10^{-4}m^{-2} \cdot sec^{-1} \cdot TeV^{-1}$ is assumed and cutoff-energies in the range from 100GeV to 1TeV are taken into account. The background is modelled by the cosmic ray background: a spectral index of -2.7 was chosen for the proton-spectrum, the flux observed from the Crab-nebula ($3.2 \cdot 10^{-7}m^{-2} \cdot sec^{-1} \cdot TeV^{-1}$) has been used in order to be able to scale the MC event rate with the scale factor obtained from Milagro MC and Milagro data. No energy cuts are applied to the proton spectrum. For different zenith angle ranges $\Delta\theta = 5^o$ the expected sensitivity of the two detector geometries to this kind of source has been estimated, the results are presented in figure 30. Since the Milagro observatory does not have an energy-scale, i.e. for data the energy of the primary is unknown, the scaling-factor k cannot be calculated for each energy bin. As an estimate the mean of 3.244 for geom04 and 4.846 for geom05 of the k-distribution calculated in subsection 7.1 has been taken.

As expected, both geometries gain sensitivity with smaller zenith angles. For all zenith angle-bands geom05 achieves higher sensitivities than geom04 at low cutoff energies. For cutoff energies larger than 400GeV, however, the behavior changes. Here geom04 leads to higher sensitivities. For geom05 the higher effective area at lower energies leads to an increase in sensitivity to sources with an energy cutoff at low energies. For high cutoff energies the higher effective area of geom04 and the smaller bin size lead to higher sensitivities. For the lowest zenith angles, however, where both geometries have their maximal effective areas, the difference in sensitivity becomes less significant and the behavior even flips for zenith angles out of the range $10^o \leq \theta \leq 35^o$ and cutoff-energies higher than 400GeV. With decreasing zenith angle and increasing cutoff-energy the performance of the two geometries becomes more and more similar. For an overhead source with a low energy-cutoff at 100GeV the flux required for a 5σ-observation around $9 \cdot 10^{-8}ergs \cdot cm^{-2}$ for geom05 and less than

$3 \cdot 10^{-7} ergs \cdot cm^{-2}$ for geom04. An overhead source with high energy-cutoff at 1TeV requires only less than $3 \cdot 10^{-8} ergs \cdot cm^{-2}$ in both geometries.

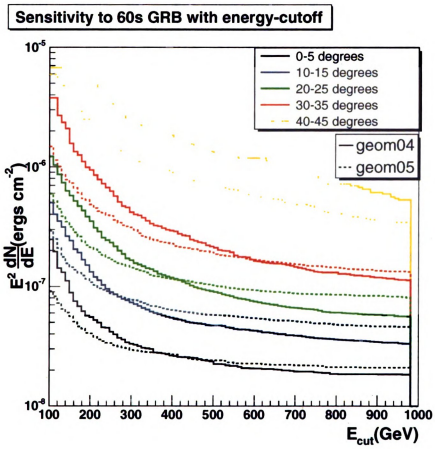

Figure 30: Flux required for a 5σ-observation of a 60s GRB versus cutoff-energy for different zenith-angle ranges for both HAWC-geometries.

GRBs have been measured in a redshift-range from z=0.008 to z=3.4. Distant sources are detected with a lower flux at earth, because on the one hand the density of photons originating from the source decreases with r^2 and on the other hand interactions with the interstellar medium lead to absorbtion. The redshift dependence of HAWCs sensitivity for a 60s GRB up to redshifts of 1.8 is shown in figure 31.

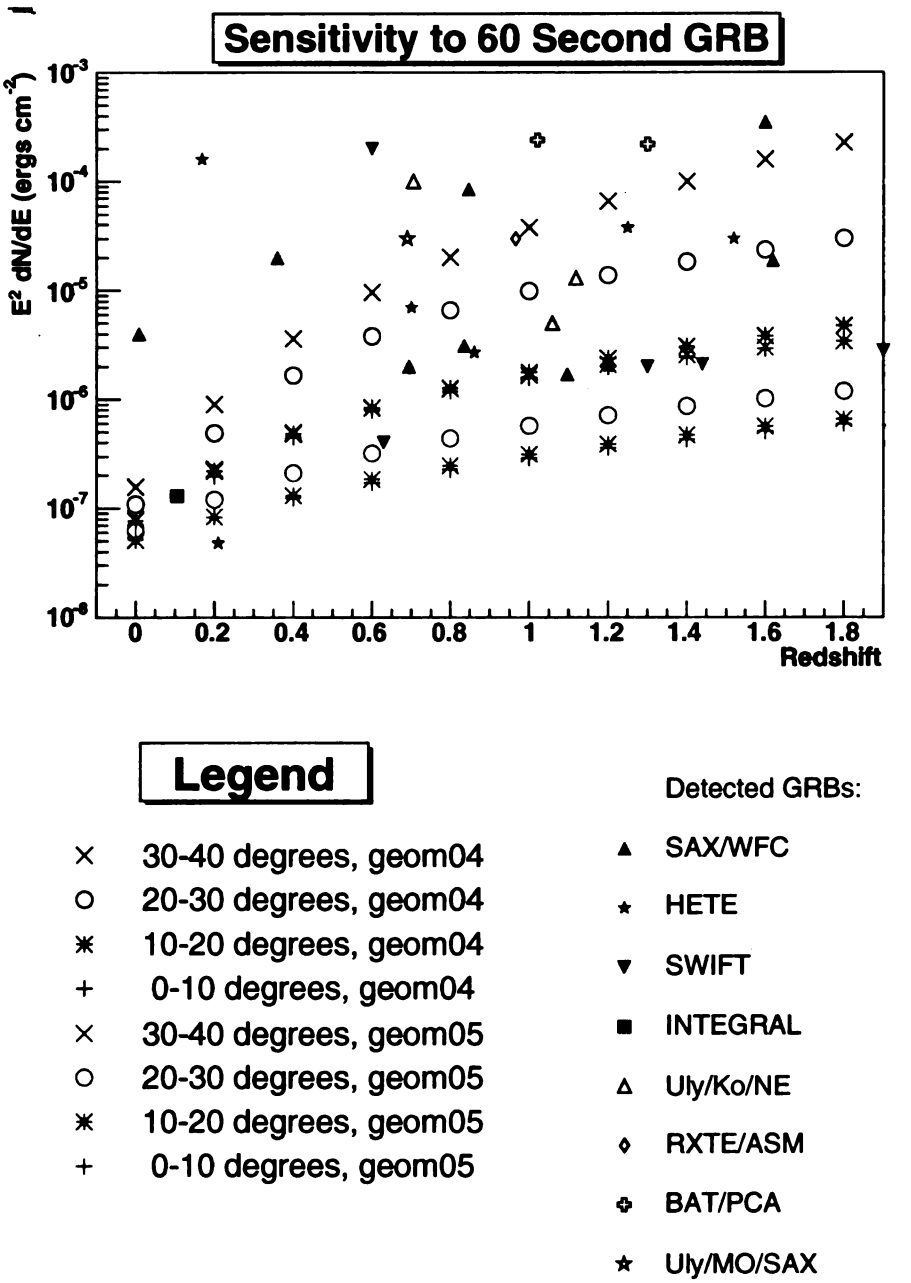

Figure 31: Flux required for a 5σ-observation of a 60 second GRB for both geometries: blue: geom04, red: geom05. Summary of detected GRBs provided by Gus Sinnis, localizing instruments taken from [20].

The two lowest zenith angle-bands $0^o \leq \theta \leq 10^o$ and $10^o \leq \theta \leq 20^o$ perform nearly identical for low redshifts: For a local source (z=0) a flux of about $5.4 \cdot 10^{-8} ergs \cdot cm^{-2}$ is required in order to observe the source at the 5σ-level for geom05 and $7.2 \cdot 10^{-8} ergs \cdot cm^{-2}$ are required for geom04. With growing distance the difference in sensitivity between the declination bands becomes more significant, for redshifts higher than 0.8 the sensitivity in the highest zenith-angle band starts decreasing rapidly for geom04, leading to a difference in fluxes required for a 5σ observation of two orders of magnitude at a redshift of 1.8. For a 5σ observation of an overhead source at a redshift of 1 a flux of less than $3 \cdot 10^{-7} ergs \cdot cm^{-2}$ is required for geom05 and a flux of $1.6 \cdot 10^{-6} ergs \cdot cm^{-2}$ is required for geom04. Apart from one GRB at z=0.2 all detected GRBs shown in figure 31 with redshifts lower than 1.8 could have been observed by geom05 at the 5σ-level assuming they occured at zenith angles lower than 20^o. Including all zenith angles up to 40^o a fraction of 71% could have been observed at the same level in this geometry.

8 Conclusion

I have compared the performance of two possible HAWC-geometries with respect to angular resolution and optimal bin size, background rejection-capabilities and sensitivity to point sources. Compared to baffles, curtains decrease the optimal bin size by a factor of 0.8, thus leading to an improvement in angular resolution by the same factor. Two different variables for γ/hadron-separation, C_H and the combination of AX_3 and CX_2 have been examined. With baffles, Q-factors above 4 are achievable for cuts in AX_3 and CX_2, while the curtained geometry still leads to Q-factors of more than 3. Cuts in C_H lead to a Q-factor of less than 2 in the baffled geometry and above 3 in the curtained geometry.

Cuts in both variables and geometries reduce the number of lower energetic events significantly more than the number of higher energetic events, thus shifting the triggered energy spectrum towards higher energies. Similarly, the effective area is reduced mainly for lower energies due to these cuts. Despite the different cut values the baffled geometry leads to higher effective areas in nearly all energy-ranges and for all γ/p cuts.

Crab-like sources with fluxes of less than 26.2mCrab per year are observed at the 5σ-level with the baffle geometry, while curtains instead of baffles increase this sensitivity to about 23.6mCrab per year. The γ/p-separation-cuts lead to a further increase by a factor of 2.7 for geom04 and the C_H cut and a factor of 3.7 for geom05 and the AX_3 and CX_2 cut. For the curtained geometry the comparably hard C_H cut performs as good as the AX_3 and CX_2 cut in terms of sensitivity to point sources. Despite the higher effective area of geom05 baffles lead to a higher sensitivity to a Crab-like source with spectral index $-2.3 \geq \alpha \geq -2.6$. For a source spectrum with a hard cutoff above a certain energy the effect of the increase in sensitivity due to curtains instead of baffles becomes even more significant: a cutoff at 10 TeV leads to

an increase in sensitivity by a factor of less than 1.1 due to curtains instead of baffles, while a cutoff at 100 GeV leads to an increase in sensitivity by a factor of about 2.5.

Local GRBs with a duration of 60s and fluxes as low as $5.4 \cdot 10^{-8} ergs \cdot cm^{-2}$ are observed at the 5σ-level with the baffled geometry while the curtained geometry requires a flux of at least $7 \cdot 10^{-8} ergs \cdot cm^{-2}$ for the same significance. For redshifts around one fluxes between $3 \cdot 10^{-7} ergs \cdot cm^{-2}$ and $1.7 \cdot 10^{-6} ergs \cdot cm^{-2}$ are required to observe a GRB at the 5σ-level with geom05 while geom04 requires fluxes between $1.6 \cdot 10^{-6} ergs \cdot cm^{-2}$ for overhead sources and $3.8 \cdot 10^{-5} ergs \cdot cm^{-2}$ for high zenith angles. Curtains decrease the sensitivity to GRBs for redshifts larger than 0.8 and high zenith angles dramatically, for all redshifts up to 1.8 and all zenith angles baffles lead to higher sensitivities.

Curtains compared to baffles improve the background rejection capability with the variable C_H, but higher Q-factors can be achieved through cuts in AX_3 and CX_2 with baffles. Baffles lead to a higher detector efficiency, but the smaller bin size for curtains makes geom04 more sensitive to Crab-like sources. Compared to baffles, curtains improve the angular resolution, but lead to a significantly worse sensitivity to GRBs, especially for high zenith angles.

It should be noted that for this analysis two geometries with different trigger rates have been compared. Curtains compared to baffles decrease the trigger rate significantly (see section 2.2.4). For comparable statistics in the triggered events nearly two times as many thrown gamma events and more than three times as many proton events are needed for geom04. This inequality limits the range of validity of the results presented in this thesis. An equal comparison can only be accomplished under the condition that the trigger conditions are chosen in way that leads comparable trigger rates for both geometries.

References

[1] A. Abdo, "New Gamma-Hadron Separation Technique and Varables in Milagro", Milagro Internal Memos(2005).

[2] Alexandreas *et. al.* Nuclear Instruments and Methods in Physics Research Section A, **328** 570 (1993).

[3] M. Anenomori *et al.*, ApJ **525** L93 (1999).

[4] K. Asakimori *et al.*, ApJ **502** 278 (1998).

[5] R. A. Atkins *et. al*, ApJ **583** 824-832 (2003) [astro-ph/0207149].

[6] R. A. Atkins *et. al*, ApJ **595** 803 (2003).

[7] "BATSE Gamma-Ray Burst Research", www.batse.msfc.nasa.gov/batse/grb/.

[8] E. G. Berezhko *et. al*, Astropart. Phys. **7** 183 (1997).

[9] B. L. Biermann, Astron. Astrophys. **271** 649 (1993).

[10] R. Blandford, D. Eichler, Phys. Rep. bf 154 1 (1987).

[11] M. S. Briggs *et. al*, ApJ **524** 82 (1999).

[12] R. Browning, D. Ramsden and P. J. Wright, Nature bf 232 99.

[13] O. C. de Jager *et al.*, ApJ **457** 253.

[14] L. O'C. Drury, Rep. Prog. Phys. **46** 973 (1983).

[15] D. C. Ellison, ApJ **46487** 197 (1997).

[16] E. Fermi, Phys. Rev. **75** 1169 (1949).

[17] W. Galbraith, "Extensive Air Showers", London: Butterwoth Scientifinc(1958)

[18] GEANT C.P.L 1994, "GEANT Reference Manual, Version 3.21".

[19] R. J. Gould, Phys. Rev. Lett. **15** 577 (1965).

[20] J. Greiner, "GRBs localized with BSAX ot BATSE/RXTE or ASM/RXTE or IPN or HETE or INTEGRAL or SWIFT", *www.mpe.mpg.de/~jcg/grbgen.html.*

[21] Heck *et al.*, "CORSIKA: A Monte Carlo Code to Simulate Extensice Air Showers, tech report FZKA 6019".

[22] A. M. Hillas *et al.*, ApJ **503** 744.

[23] J. A. Hinton, Ph.D. thesis, University of Leeds (1998).

[24] J. V. Jelley, "Cherenkov Radiation", New York: Pergamon Press (1958).

[25] C. F. Kennel and F. V. Coronoiti, ApJ **283**, 694 (1984).

[26] B. S. Nilsen, "New Results on Cosmic Ray H and He Composition from the JACEE Collaboration", Eighteenth Texas Symposium on Relativistic Astrophysics and Cosmology /edited by A. V. Onlinto, J.A. Frieman, and D.N. Schramm. River Edge, N.J.: World Scientific, (1998).

[27] "Picture and Plot Database", High Energy Astrophysics, University of Leeds, *www.ast.leeds.ac.uk/ ~ caw/pic_base/pic.html*.

[28] I. S. Shklovsky, "Supernovae", New York: Wiley-Interscience (1968).

[29] G. Sinnis, A. Smith and J. E. McEnery, AIP **745** 234S (2004) [arXiv:astro-ph/0403096v1].

[30] T. C. Weekes, "Very High Energy Gamma-Ray Astronomy", Institute of Physics Publishing (2003).